Theses and Dissertations             1. Thesis and Dissertation Collection, all items

2019-06

# FLUID-STRUCTURE ANALYSIS OF A TRANSONIC ROTOR

## Thornton, Grant D.

Monterey, CA; Naval Postgraduate School

https://hdl.handle.net/10945/62704

# NAVAL POSTGRADUATE SCHOOL

### MONTEREY, CALIFORNIA

# THESIS

**FLUID-STRUCTURE ANALYSIS OF A TRANSONIC ROTOR**

by

Grant D. Thornton

June 2019

Thesis Advisor: Anthony J. Gannon
Co-Advisor: Garth V. Hobson

**Approved for public release. Distribution is unlimited.**

THIS PAGE INTENTIONALLY LEFT BLANK

| REPORT DOCUMENTATION PAGE | *Form Approved OMB No. 0704-0188* |
|---|---|

Public reporting burden for this collection of information is estimated to average 1 hour per response, including the time for reviewing instruction, searching existing data sources, gathering and maintaining the data needed, and completing and reviewing the collection of information. Send comments regarding this burden estimate or any other aspect of this collection of information, including suggestions for reducing this burden, to Washington headquarters Services, Directorate for Information Operations and Reports, 1215 Jefferson Davis Highway, Suite 1204, Arlington, VA 22202-4302, and to the Office of Management and Budget, Paperwork Reduction Project (0704-0188) Washington, DC 20503.

| 1. AGENCY USE ONLY *(Leave blank)* | 2. REPORT DATE<br>June 2019 | 3. REPORT TYPE AND DATES COVERED<br>Master's thesis |
|---|---|---|

| 4. TITLE AND SUBTITLE<br>FLUID-STRUCTURE ANALYSIS OF A TRANSONIC ROTOR | 5. FUNDING NUMBERS |
|---|---|
| **6. AUTHOR(S)** Grant D. Thornton | |

| 7. PERFORMING ORGANIZATION NAME(S) AND ADDRESS(ES)<br>Naval Postgraduate School<br>Monterey, CA 93943-5000 | 8. PERFORMING ORGANIZATION REPORT NUMBER |
|---|---|

| 9. SPONSORING / MONITORING AGENCY NAME(S) AND ADDRESS(ES)<br>Office of Naval Research | 10. SPONSORING / MONITORING AGENCY REPORT NUMBER |
|---|---|

**11. SUPPLEMENTARY NOTES** The views expressed in this thesis are those of the author and do not reflect the official policy or position of the Department of Defense or the U.S. Government.

| 12a. DISTRIBUTION / AVAILABILITY STATEMENT<br>Approved for public release. Distribution is unlimited. | 12b. DISTRIBUTION CODE<br>A |
|---|---|

**13. ABSTRACT (maximum 200 words)**

This study developed and applied a 2-way fluid-structure interaction model to increase fidelity in numerical simulations of the Naval Postgraduate School Military Fan. The Naval Postgraduate School Military Fan is an existing transonic-rotor geometry undergoing test and evaluation using the Turbopropulsion Lab's Transonic-Compressor Rig.

A fluid solution using ANSYS CFX was developed and coupled with an ANSYS Mechanical static-structural solution of the rotor blade to model the hot shape of the rotor. Cold-shape simulations were conducted for 0.42% average blade-height (0.381 mm) and 1.41% average blade-height (1.27 mm) tip-gap configurations, and hot-shape simulations were conducted for the latter configuration. Performance predictions in terms of total pressure ratios and isentropic efficiencies were compared for cold- and hot-shape analyses and measured for fidelity against experimental data. Hot-shape analyses consistently improved modeling fidelity as compared to cold-shape analyses by allowing for increased mass-flow rates due to radial growth and untwist of the rotor blades at speed. Flow features associated with the transonic regime were identified and discussed for both cold and hot analyses.

With the developed experimentally verified modeling procedure, CFD predictions may be conducted for alternate configurations of the evaluated rotor or for other transonic rotor geometries as a supplement to experimental data acquisition.

| 14. SUBJECT TERMS<br>transonic rotor, CFD, CFX, fluid-structure interaction, tip-gap effects, tip-leakage vortex | 15. NUMBER OF PAGES<br>91 |
|---|---|
| | 16. PRICE CODE |

| 17. SECURITY CLASSIFICATION OF REPORT<br>Unclassified | 18. SECURITY CLASSIFICATION OF THIS PAGE<br>Unclassified | 19. SECURITY CLASSIFICATION OF ABSTRACT<br>Unclassified | 20. LIMITATION OF ABSTRACT<br>UU |
|---|---|---|---|

NSN 7540-01-280-5500

Standard Form 298 (Rev. 2-89)
Prescribed by ANSI Std. 239-18

THIS PAGE INTENTIONALLY LEFT BLANK

**FLUID-STRUCTURE ANALYSIS OF A TRANSONIC ROTOR**

Grant D. Thornton
Ensign, United States Navy
BSAE, U.S. Naval Academy, 2018

Submitted in partial fulfillment of the
requirements for the degree of

**MASTER OF SCIENCE IN ENGINEERING SCIENCE
(AEROSPACE ENGINEERING)**

from the

**NAVAL POSTGRADUATE SCHOOL
June 2019**

Approved by:      Anthony J. Gannon
Advisor

Garth V. Hobson
Co-Advisor

Garth V. Hobson
Chair, Department of Mechanical and Aerospace Engineering

THIS PAGE INTENTIONALLY LEFT BLANK

# ABSTRACT

This study developed and applied a 2-way fluid-structure interaction model to increase fidelity in numerical simulations of the Naval Postgraduate School Military Fan. The Naval Postgraduate School Military Fan is an existing transonic-rotor geometry undergoing test and evaluation using the Turbopropulsion Lab's Transonic-Compressor Rig.

A fluid solution using ANSYS CFX was developed and coupled with an ANSYS Mechanical static-structural solution of the rotor blade to model the hot shape of the rotor. Cold-shape simulations were conducted for 0.42% average blade-height (0.381 mm) and 1.41% average blade-height (1.27 mm) tip-gap configurations, and hot-shape simulations were conducted for the latter configuration. Performance predictions in terms of total pressure ratios and isentropic efficiencies were compared for cold- and hot-shape analyses and measured for fidelity against experimental data. Hot-shape analyses consistently improved modeling fidelity as compared to cold-shape analyses by allowing for increased mass-flow rates due to radial growth and untwist of the rotor blades at speed. Flow features associated with the transonic regime were identified and discussed for both cold and hot analyses.

With the developed experimentally verified modeling procedure, CFD predictions may be conducted for alternate configurations of the evaluated rotor or for other transonic rotor geometries as a supplement to experimental data acquisition.

THIS PAGE INTENTIONALLY LEFT BLANK

# TABLE OF CONTENTS

# LIST OF FIGURES

# LIST OF TABLES

THIS PAGE INTENTIONALLY LEFT BLANK

# LIST OF ACRONYMS AND ABBREVIATIONS

CATG            cells across the gap

CFD             computational fluid dynamics

FSI             fluid-structure interaction

LE              leading edge

NPS             Naval Postgraduate School

NPSMF           Naval Postgraduate School military fan

SST             shear stress transport

TCR             transonic compressor rig

TE              trailing edge

Ti-64           titanium alloy Ti-6Al-4V

TPL             Turbopropulsion Laboratory

THIS PAGE INTENTIONALLY LEFT BLANK

# ACKNOWLEDGMENTS

THIS PAGE INTENTIONALLY LEFT BLANK

# I. INTRODUCTION

## A. MOTIVATION

The Naval Postgraduate School (NPS) Turbopropulsion Laboratory (TPL) is currently testing a transonic-rotor geometry known as the NPS military fan (NPSMF) using the TPL's transonic compressor rig (TCR). Current tests focus on evaluating rotor performance at a variety of operating conditions as well as determining rotor growth. Each test is costly due to the power required to operate the NPSMF at speed. A computational model that could adequately replicate and predict rotor performance would significantly reduce cost, time, and risk involved in the test and evaluation of the NPSMF and other transonic-rotor geometries. Additionally, aerodynamic and structural phenomena not observable in an experimental setting could be identified and evaluated.

Current computational fluid dynamics (CFD) models lack significant fidelity in modeling the NPSMF to replicate experimental data. One attributing factor is that they operate using the "cold" shape of the rotor. During operation, rotational and fluid interaction loads radially grow and untwist each blade of the rotor allowing for increased mass-flow rates and changes in performance of the rotor. Coupling of a fluid model for pressure loading on the blade with a structural model of blade deflection through a fluid-structure interaction (FSI) could increase fidelity in a CFD model's ability to capture the rotor's deflection and performance. An experimentally verified CFD model for one or more test configurations could be further applied to predict performance in alternate configurations at a fraction of the time and cost required for full-scale testing.

## B. PREVIOUS WORK

Previous modeling of the NPSMF utilized the cold shape of the blade with a decreased tip-gap to compensate for the average radial growth due to rotational loads [1]. This approach allows for first-order approximation of tip-gap effects but fails to account for blade "untwisting" and non-uniform radial growth that occurs due to rotational and fluid-interaction loads.

1

A modal analysis was conducted for the NPSMF in which the various vibrational modes resultant from rotation of the blade and combined disk (blisk) were analyzed [2]. The current study does not focus on transient vibrational modes, rather it focuses on the steady-state solution of structural deformation. The previous study modeled the entire rotor-blisk assembly and thus required a relatively coarse mesh; this study limits the structural geometry to the rotor blades and utilizes increased refinement in the structural mesh to account for the fluid-structural interface. In addition, the previous study did not account for forces caused by a fluid interaction, whereas the current study accounts for deformation due to both fluid interaction and axial rotation.

The TPL has applied a 2-way FSI to a splittered-rotor geometry with moderate success as discussed by Terrell [3]. The current study applies a model of only one blade passage with a tip-gap to allow for increased mesh refinement at the same or lower computational cost. Results in Terrell's study showed an extension in predicted stall margin for the hot shape as opposed to the cold for that rotor geometry. Also, Terrell implemented the shear-stress-transport (SST) turbulence model with a gamma-theta transitional-turbulence model, which shifted data trends towards experimental results, increasing modeling fidelity. This study implements the same turbulence models with lower values of y+, the non-dimensional distance from the wall to the first grid point, to increase model fidelity, as recommended by Terrell [3].

## C.    CURRENT STUDY

This research aims to increase computational-modeling fidelity of the NPSMF through development and implementation of a coupled FSI model. The model employs the System Coupling tools in ANSYS Workbench to couple a CFX fluid simulation with an ANSYS Mechanical structural model of the rotor blades. Each component of the coupled model was verified prior to implementation in a full 2-way coupled analysis to reduce risk of failure in full-scale simulations. Once the coupled model was functional for single-point acquisition, it was applied to predict a full speed-line and compared to experimental data for assessment of modeling fidelity. Through experimental validation, a modeling procedure could be used to predict performance of other transonic-rotor geometries with a

reduced or removed requirement for costly experimentation. Additionally, novel configuration modifications could be modelled with greater certainty prior to testing and implementation.

THIS PAGE INTENTIONALLY LEFT BLANK

# II. EXPERIMENTAL FACILITY AND PROCEDURES

Experimental values of performance parameters for the NPSMF were obtained at the NPS TPL using the TCR. Tests of interest for this study were conducted at 27,000 RPM or 90% of the design speed of the NPSMF (30,000 RPM). Matching the results from experimental test and evaluation was the ultimate objective for computational-model fidelity in this research.

## A. TRANSONIC COMPRESSOR RIG

The TPL's TCR is used to evaluate performance of high-speed turbomachinery. A complete description of the TCR may be found in the studies of Descovitch [4], DeSousa [1], and McNab [2]. Experimental data for this study utilized the rotor-only setup shown in Figure 1 with a smooth traditionally machined casing, as discussed in DeSousa [1].
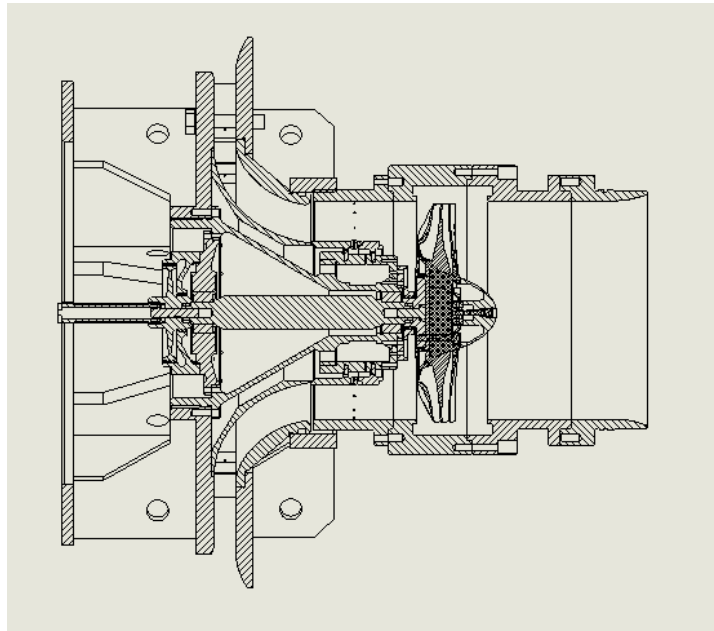


Figure 1.    TCR engineering drawing profile view. Source: [1].

Two configurations of relevance are referenced in this study: a tight tip-gap configuration (approximately a 0.381 mm or 0.015 in. cold tip clearance) and a large tip-

gap configuration (approximately a 1.27 mm or 0.050 in. cold tip clearance). These correspond to 0.42% and 1.41% of the mean blade height respectively. While the tight configuration better represents practical performance of the NPSMF, the large tip-gap configuration lends itself to better FSI modeling due to mesh shearing concerns in the tip-gap region. Thus, tight tip-gap experimental data was used as the baseline for preliminary cold-shape analyses, and large tip-gap data was used as the baseline for 2-way FSI predictions.

Upstream of the test section shown in Figure 1, the TCR utilizes a mass-flow nozzle to calculate the experimental mass-flow rate based upon pressure and temperature probe measurements as shown in Figure 2. The mass-flow nozzle of the TCR was of particular interest in this research due to its recorded discharge coefficient ($C_D$) of 1.03 and concerns over experimental mass-flow rates being larger than preliminary CFD predictions. A full CFD analysis was conducted at various operating conditions and verified this value for $C_D$, as discussed in Appendix A.
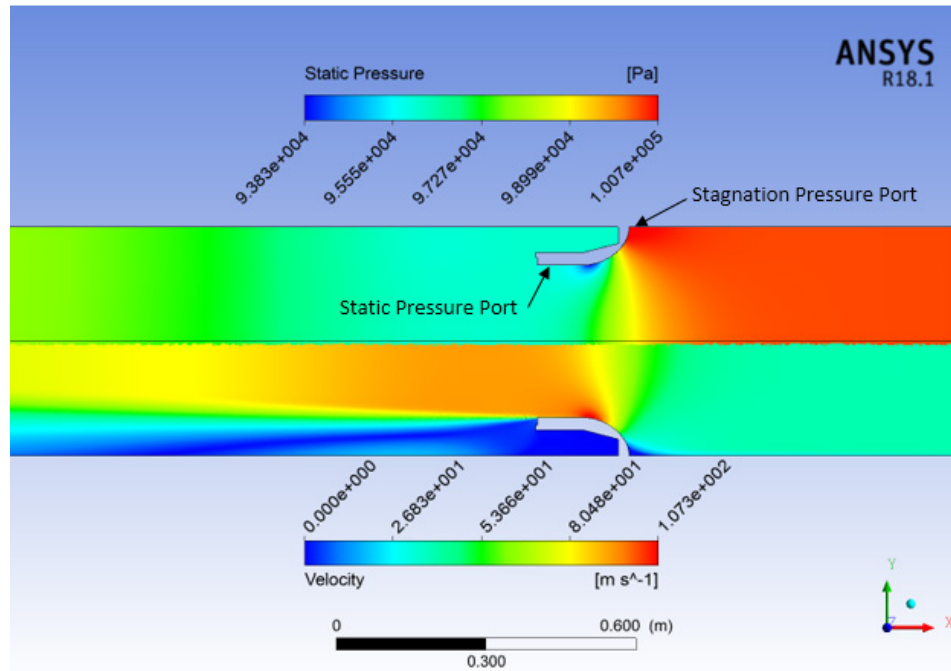


Figure 2.    Model of mass-flow nozzle for TCR

## B. EXPERIMENTAL DATA ACQUISITION AND REDUCTION

Experimental evaluation of a speed-line using the TCR involves first bringing the rotor to the desired speed at fully open throttle. Then, the throttle is iteratively closed to decrease the mass flow through the TCR with steady-state data recorded at each throttle condition. If testing is to be conducted through stall, minor closures of the throttle are made in the near-stall region until the rotor stalls.

Recorded data includes probe measurements from the mass-flow nozzle, two rotor-inlet pressure probes and thermocouples, and pressure probes and thermocouples placed at varying radial position in the outlet plane downstream of the tested rotor. Additional recorded data includes rotor RPM and atmospheric conditions for humidity corrections on the day of testing. These pressure and temperature measurements are mass-averaged and used to define performance parameters based upon the relationships described in McNab [2] and Descovich [4]. Particular performance parameters of interest to this study were total pressure ratio, isentropic efficiency, and mass-flow rate.

Accumulated error through the data-acquisition and reduction process was of particular concern for modeling fidelity in this study. Thus, a mathematical analysis of the normalized error for mass-flow rate at a single point was conducted and placed in Appendix B. This error analysis produced error bars based upon the normalized error for each test measurement as shown in Figure 3. Steps of normalized error from experimental data to CFD predictions served as a metric of computational-model fidelity for this study.
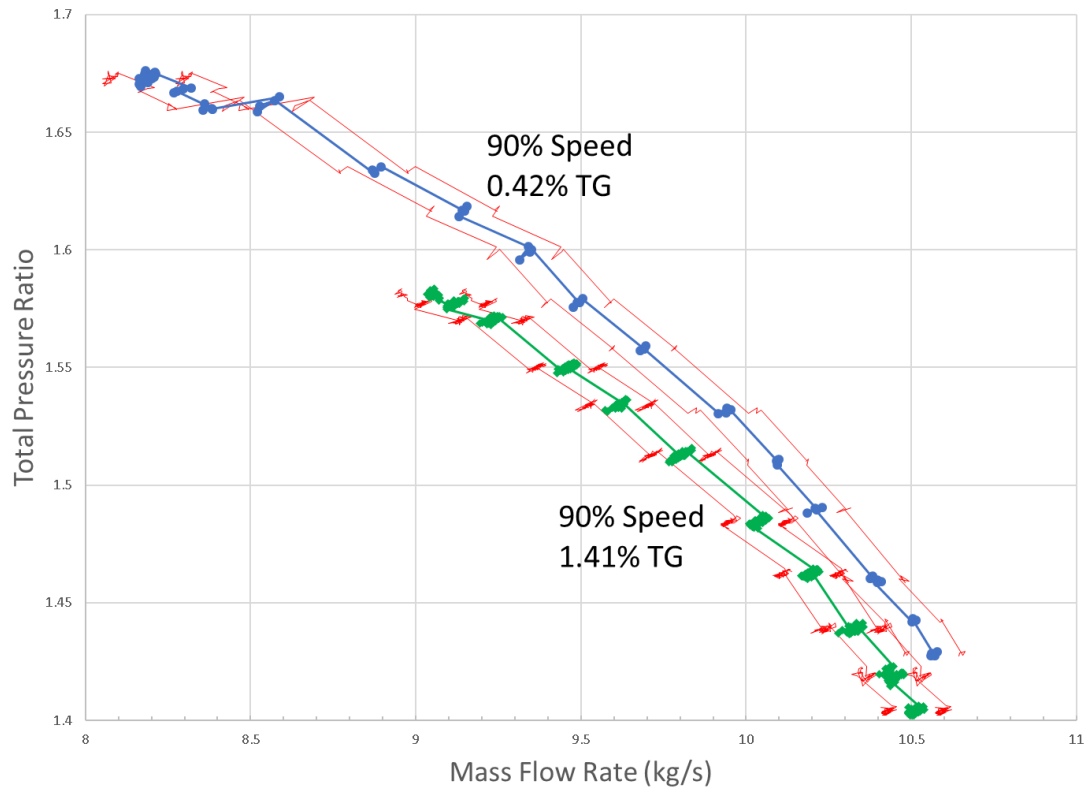
Figure 3.    Experimental pressure ratios with applied error bars

# III.   COMPUTATIONAL MODELING

Computational modeling for a FSI of the NPSMF involved the following approach: construct rotor and gas-path geometries; develop a fluid model in CFX; develop structural model in ANSYS Mechanical; and couple the two using the built in System Coupling Tool. Parameterization was applied within each module according to the procedure described in Appendix C. Details of the Workbench-model construction and assumptions made therein are discussed in this chapter.

## A.   ROTOR GEOMETRY

The NPSMF is a 20-blade transonic-rotor blisk made of Ti-64 currently undergoing testing at the TPL. Its geometric model was made using geometric splines and lofted surfaces in Solidworks to match the constructed-blisk geometry. To model the fluid flow around the rotating-blisk geometry, an 18-degree wedge was constructed to match the geometry of the test section of the TCR by McNab [2] and subsequently modified by DeSousa [1] to reflect changes in the TCR test section. The gas-path wedge was modified in this study to construct two gas paths: a tight tip-gap gas path of 0.1778 mm (0.007 in.) to match the tight tip-gap configuration minus the average predicted radial growth as done by DeSousa [1], and a large tip-gap 1.27 mm (0.050 in.) to match the large tip-gap configuration. The rotor-blisk geometry was then subtracted from this control volume using Design Modeler to make the single-blade gas path used for the fluid analysis as shown in Figure 4.
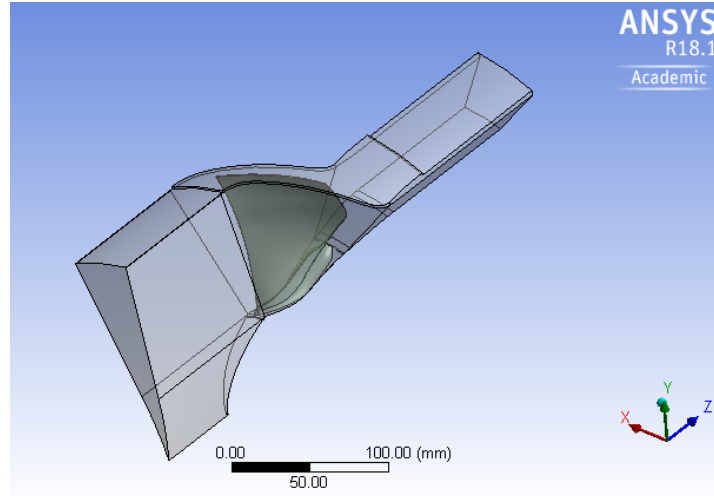
Figure 4. Gas-path geometry with sliced blisk

**B. CFX FLUID ANALYSIS**

**1. Mesh**

The developed gas path was implemented into the meshing cellblock for a CFX fluid-flow analysis. A patch-conforming mesh of tetrahedrons was used with sets of inflation layers for all wall surfaces such as the blisk and the counter-rotating walls.

**2. CFX-Pre Setup**

For the fluid-solver analysis, the SST turbulence model was used along with the gamma-theta transitional-turbulence model. Inlet stagnation pressure and temperature as well as outlet average static pressure served as the boundary conditions for numerical simulation. The sides of the gas-path wedge served as periodic boundary conditions. The blade surface served as the FSI surface.

Mesh deformation was enabled with mesh stiffness defined as a blended function of distance and small cell volumes. The NPSMF blade surface was set to receive mesh deformation and send force data with wall velocity set relative to mesh motion. The casing surface, the outer wall in the tip-gap region, allowed mesh deformation only in the revolutionary direction (i.e., along the outer wall) to relax mesh shearing in the tip-gap region. Here the wall velocity was set to be relative to the boundary condition.

10

Calculation of speed-lines was conducted by varying pressure conditions either at the inlet or at the outlet of the gas path. As the objective of this study was to predict rotor performance, experimental conditions were not used to define the boundary conditions for CFX-Pre. Instead, varying outlet average static pressure with inlet stagnation pressure at the reference condition was the standard approach used in the study. Benefits of this approach were that no mass-flow correction had to occur to scale the results to reference conditions; detriments included slower convergence as the boundary conditions had to pass upstream through the gas path. An alternative approach was to iteratively lower the inlet stagnation pressure with outlet average static pressure held constant. While this adds the requirement to scale results to reference conditions, it better matches the procedure conducted in experiment: iteratively throttling at the inlet and expanding to near atmospheric conditions at the outlet. This procedure could better account for Reynolds-number effects closer to the near-stall region of the speed-line as compared to the outlet static-pressure approach. However due to the additional scaling requirement, speed-lines predicted in this study were calculated by varying the outlet static pressure.

## C.    ANSYS MECHANICAL STATIC-STRUCTURAL ANALYSIS

### 1.    Geometry and Mesh

The structural analysis in this study only incorporated effects seen by the rotor blade rather than the entire blisk as shown by the constructed geometry with applied mesh in Figure 5. A comparison between entire blisk and rotor-blade deformation is discussed later in this report. Only using the blade reduced complexity in the structural analysis and reduced the number of surfaces connected through the FSI. The applied mesh focused on maintaining high resolution along the edges of the blade to maintain integrity in modeling the curvature of the blade during the mesh-deformation data transfer.
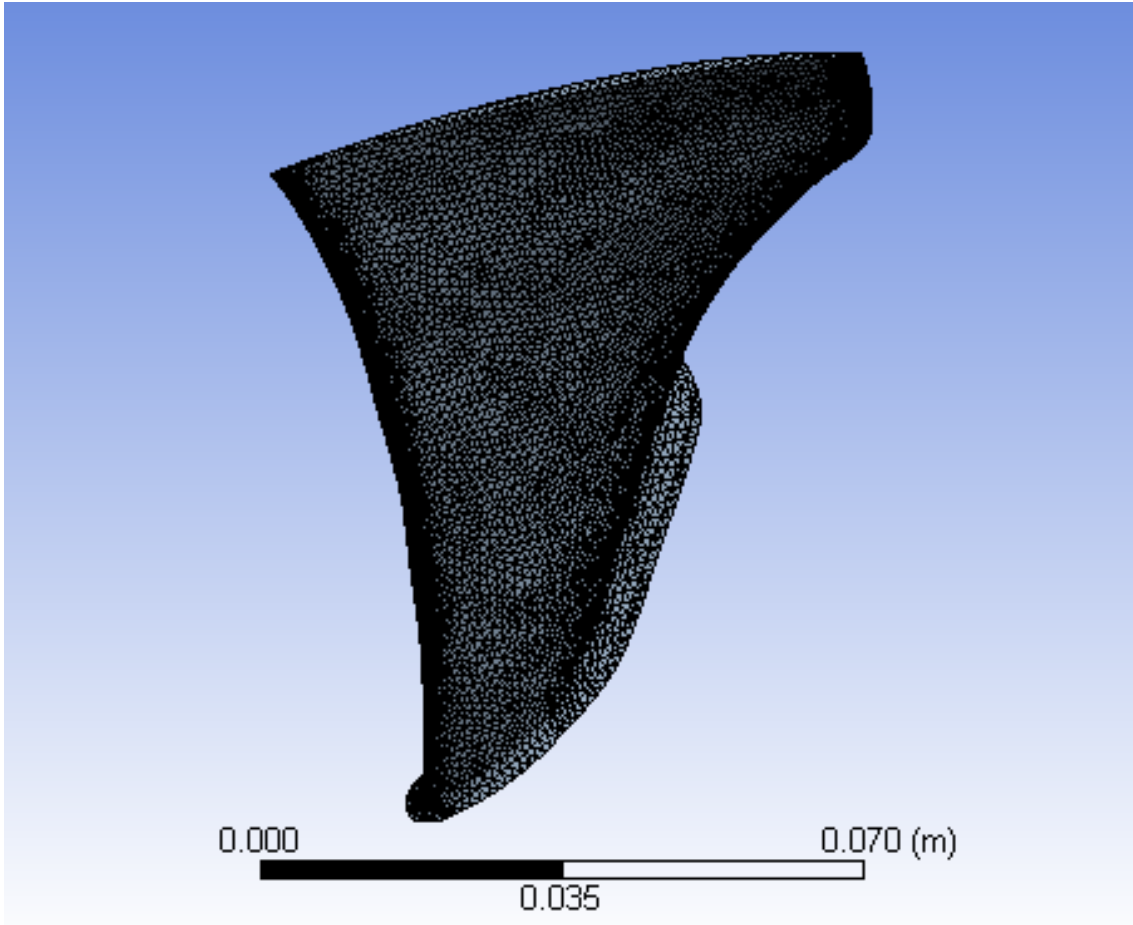
Figure 5.    Meshed rotor-blade geometry

## 2.    Analysis Setup

The ANSYS Mechanical portion of the FSI was conducted as a static-structural analysis to promote convergence to a steady-state solution. Boundary conditions for the test case involved setting the base of the rotor blade as a fixed support, applying a ramped rotational velocity of 27000 RPM about the axial axis, and setting a fluid-interaction surface for all other blade surfaces.

## 3.    Deformation Due to Rotational Velocity

A preliminary analysis was conducted of deformation of the NPSMF solely due to rotational velocity to provide a baseline prior to FSI and to validate the structural model. The results for total deformation are shown in Figure 6. These results showed a slight

12

increase in deformation than seen in previous analyses for the entire blisk [2], but were deemed accurate enough for the current analysis. Blade deformation is further discussed alongside 1-way and 2-way FSI results.
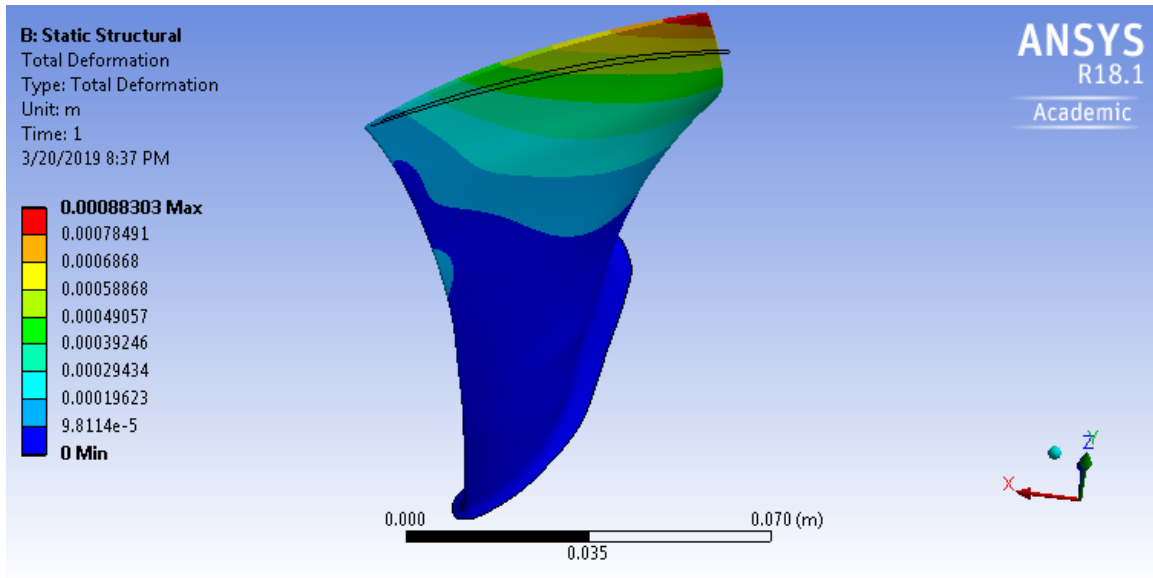


Figure 6.     Total deformation due to 90% speed operation

## D.     SYSTEM COUPLING

The setup blocks of CFX and ANSYS Mechanical were fed to the setup block of System Coupling. Within System Coupling, the force and deformation data transfers were defined with appropriate ramping, and the coupling-iteration number and stagger order were set. The resultant Workbench architecture is shown in Figure 7. Further discussion of setup and application of System Coupling was placed in Appendix D.
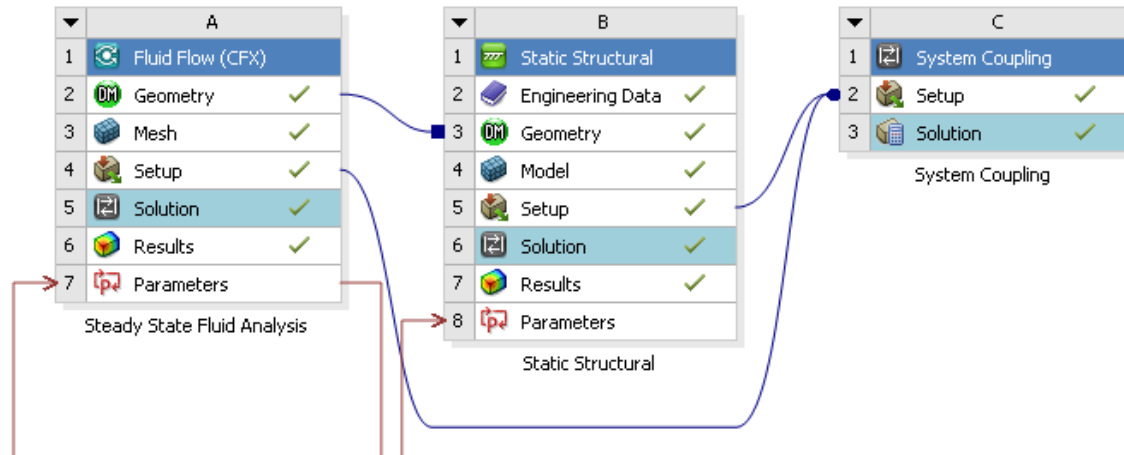
Figure 7.    Workbench architecture for System Coupling

## E.    RISK REDUCTION APPROACH

Due to the computational cost and modeling complexity of a coupled analysis, the component-based validation procedure shown in Table 1 was used. This iterative approach to developing the 2-way FSI allowed for experience with, validation of, and intermediate results from each component of the FSI prior to full-scale simulation at a refined mesh.

Table 1.    Risk reduction approach

| Component | Validation Approach | Results |
|---|---|---|
| CFX Fluid Solver | Stand-alone Cold-Shape Analysis | Validation of meshing approach and solver metrics Baseline Tight-TG CFD results |
| Static Structural | Stand-alone Rotational Deformation only | Validation of structural solver metrics and boundary conditions Baseline Deformation Results |
| Fluid-Load Data Transfer | 1-Way FSI | $1^{st}$ order FSI only and Rotation plus FSI results |
| Deformation Data Transfer | Mesh motion enabled without any data transfer, then deformation data transfer only | Intermediate validation of mesh deformation in CFX, defined stagger iteration approach (no recorded results) |
| 2-Way FSI | Coarse 2-Way FSI | Validation of 2-way FSI convergence, added conservation convergence criteria, affirmation of chosen turbulence model |

# IV. COLD-SHAPE ANALYSIS RESULTS

The CFX fluid-model was first verified with a cold-shape analysis of the NPSMF. This enabled refinement iterations of mesh metrics to be done separate from the long runtimes required for FSI, and it enabled the establishment of baseline fidelity in computational ability to predict rotor performance as applied for the tight tip-gap configuration.

## A. MODEL SETUP

Several iterations of a cold-shape analysis were conducted to provide experience with meshing and modeling strategies for the NPSMF and its gas path. The final refined mesh used in cold-shape analysis prior to focusing on coupled analyses is shown in Figure 8 with mesh statistics documented in Table 2. Further refinement was limited by computational resources available and time required to adequately focus on the FSI.
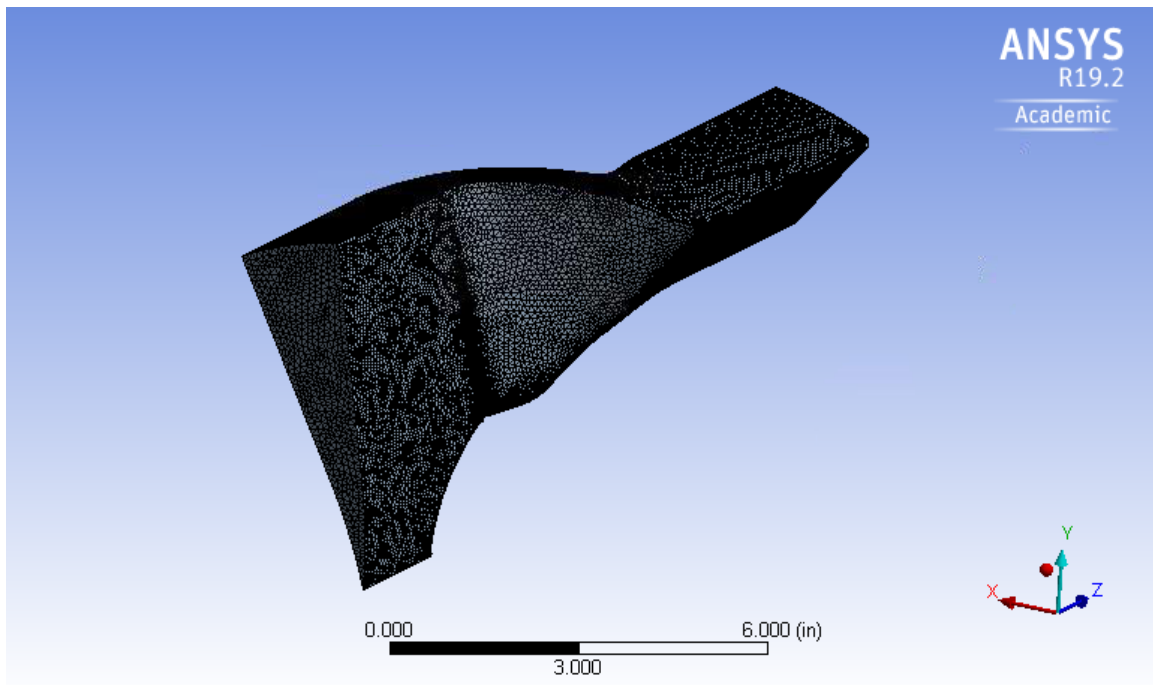


Figure 8.  Refined mesh used for cold-shape analysis

Table 2.    Mesh statistics for cold-shape analysis

|  | CFX Fluid Analysis |
|---|---|
| Mesh Nodes | 3,605,192 |
| Mesh Elements | 9,404,749 |

The meshing approach for this study involved using a patch-conforming mesh of tetrahedrons. Edge refinement was applied to the rotor blade at the tip as well as the leading and trailing edges. Inflation layers were defined for each surface other than the periodic boundaries, inlet, and outlet. These inflation layers were defined based upon first-layer thickness and number of layers. This allowed for simple modification of the mesh to match desired y+ values based upon average values recorded from preliminary simulations at near-choke conditions.

## B.    PREDICTED PERFORMANCE

The generated mesh for the gas path was used to predict a 90% speed-line of the NPSMF in a tight tip-gap configuration by iteratively raising the average backpressure. A setup report of all applied settings for CFX-Pre was placed in Appendix E, and notes on domain initialization for this flow regime were placed in Appendix F.

### 1.    Total Pressure Ratio

The predicted total pressure ratio at 90% speed is plotted against the corrected mass-flow rate in Figure 9 alongside the experimental data with error bars applied. The cold-shape analysis appears to match experimental trends but at a lower mass-flow rate. Numerically, computational predictions under predicted mass flow by approximately 5.43 steps of the normalized error at near-choke conditions and 3.13 steps of the normalized error near the stall condition. Steps of normalized error were defined by the addition or subtraction of normalized error from the nearest pressure-ratio matching experimental data point. Factors attributed to this difference in mass flow could include need for further mesh refinement, inappropriate boundary conditions, and deformation of the rotor at 90% speed. Boundary conditions may be improved by applying a lower or zero value blending factor

for the average pressure outlet. This would only enforce the average value on the outlet and result in freedom for substantial fluctuation in pressure and thus a more realistic plot of the outlet at the cost of increased convergence time. As the outlet was substantially downstream of the rotor, the default blending profile was deemed appropriate to promote faster convergence. CFD analysis also over predicts the stall margin of the NPSMF. This was also attributed to the aforementioned factors.
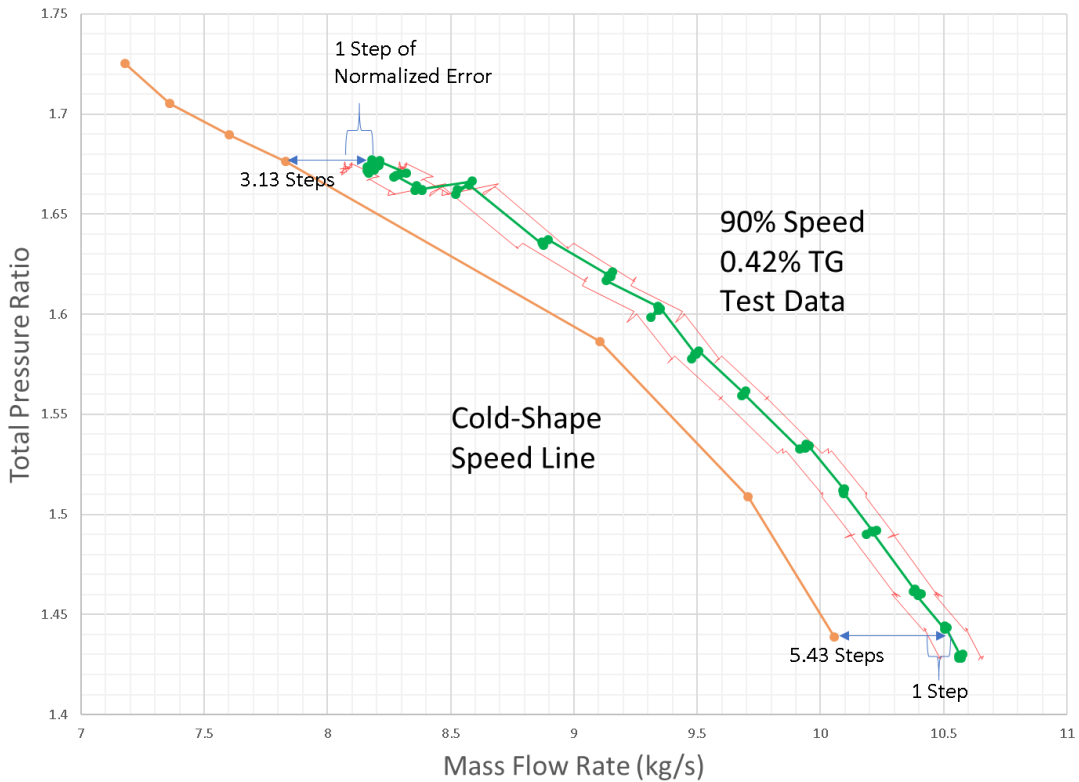


Figure 9.    Pressure ratio for cold-shape analysis

### 2.    Isentropic Efficiency

The predicted total pressure ratio at 90% speed is plotted against the corrected mass-flow rate in Figure 10 alongside experimental data. The cold-shape analysis appears to overpredict efficiencies by up to approximately 4% at a lower mass-flow rate. This difference is attributed to rotor deformation and inappropriate boundary conditions. Mesh refinement was not a key factor in this error as preliminary runs showed increased

efficiencies with further refinement. However, as mesh refinement during this phase was solely based upon y+ or first layer thickness of inflation layers, coarse meshing away from boundaries may have washed out the majority of the rotor wake before the outlet plane. This effect was taken into consideration when developing the mesh for the 2-way FSI. Boundary conditions could be improved through the introduction of heat transfer between the fluid and the walls of the domain.
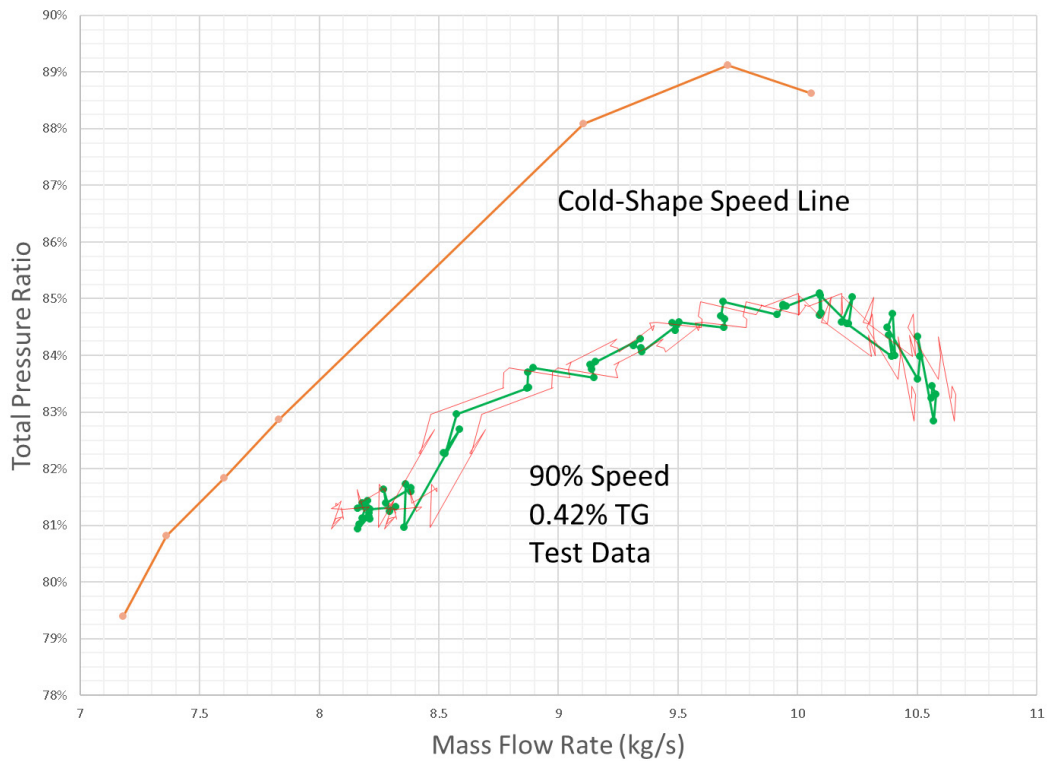


Figure 10.   Isentropic efficiency for cold-shape analysis

# V. 1-WAY FSI ANALYSIS

To validate the fluid-load data transfer of System Coupling from CFX to ANSYS Mechanical, a 1-way FSI was conducted to evaluate a first-order approximation of blade deformation due to rotation and fluid loads calculated in the cold-shape analysis. This also allowed for verification of functionality of CFX when connected to System Coupling. The model and results of this data transfer are discussed in this chapter.

## A. MODEL SETUP FOR 1-WAY FSI DATA POINT

Chosen boundary conditions and model statistics are placed in Table 3. These boundary conditions place the blade in the near-peak efficiency region of a 90% speed-line.

Table 3. Model conditions and statistics for 1-way FSI

|  | CFX Fluid Analysis | Static-Structural Analysis |
|---|---|---|
| Mesh Nodes | 2,148,616 | 1,327,022 |
| Mesh Elements | 5,560,924 | 894,370 |
| Boundary Conditions | Inlet Stagnation Pressure = 1 atm Stagnation Temp = 288.15 K Outlet Average Pressure = 1 atm | 27000 RPM Rotational Velocity, Fixed Bottom, FSI Surface |

## B. BLADE-DEFORMATION RESULTS

The total deformation of the blade due to the 1-way FSI is shown in Figure 11, and the radial deformation is shown in Figure 12.
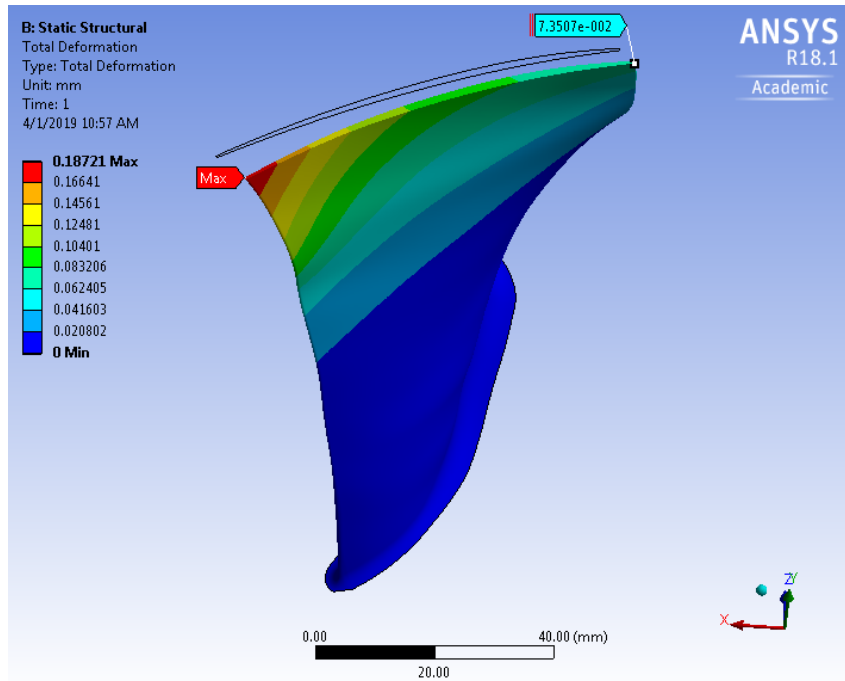
Figure 11.    Total deformation due to 1-way FSI only
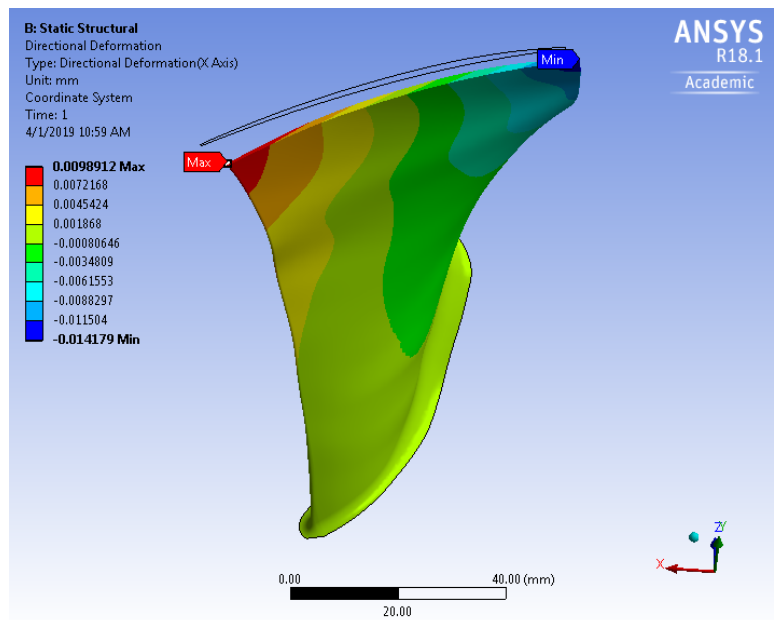


Figure 12.    Radial deformation due to 1-way FSI only

Selected results for deformation were placed in Table 4. The 1-way FSI appears to counter the deformation caused by rotation at the trailing edge (TE) of the blade, while

supplying greater deformation of the leading edge (LE) as compared to pure rotation. This resulted in a nearly linear addition of the two sources of deformation in all areas except total deformation of the LE. These results generally match with expectations for the given geometry and pressure profile, and validate the fluid-load data transfer in System Coupling. Of note, this structural model over predicts radial growth of the TE and under predicts radial growth of the LE as compared to full-blisk models [1, 2]. This was attributed to the fixed boundary condition at the root of the blade. The actual blisk would allow for some of that angular deformation to be distributed along the full length of the blade as opposed to mainly at the radial tip and thus reduce radial growth of the TE. As the average value of radial growth for the whole blade was deemed sufficiently accurate in comparison to experiment, the static-structural model was deemed adequate for the purposes of this study.

Table 4.    Deformation results for 1-way FSI

|  | Rotation only | 1-Way FSI Only | Rotation + 1-Way FSI |
|---|---|---|---|
| Max Total Deformation | 0.88304 mm (TE) (0.034765 in) | 0.18721 mm (LE) (0.0073706 in) | 0.81495 mm (TE) (0.032085 in) |
| Max Radial Growth | 0.23404 mm (TE) (0.0092141 in) | 0.0098912 mm (0.00038942 in) | 0.21986 mm (0.008656 in) |
| Total Deformation LE | 0.14775 mm (0.0058169 in) | 0.18721 mm (0.0073706 in) | 0.23563 mm (0.0092768 in) |
| Radial Growth LE | 0.036406 mm (0.0014333 in) | 0.0098912 mm (0.00038942 in) | 0.045724 mm (0.0018002 in) |
| Total Deformation TE | 0.88304 mm (0.034765 in) | 0.073507 mm (0.0028940 in) | 0.81495 mm (0.032085 in) |
| Radial Growth TE | 0.23404 mm (0.0092141 in) | -0.014179 mm (-0.00055821 in) | 0.21986 mm (0.008656 in) |

THIS PAGE INTENTIONALLY LEFT BLANK

# VI. 2-WAY FSI RESULTS

With verification of individual components and 1-way data transfers, verification of the 2-way FSI was conducted alongside a fluid-model verification analysis, which is documented in Appendix G. The result of this analysis affirmed the choice of the SST turbulence model with a gamma-theta transitional-turbulence model, which was suggested by Terrell [3]. The developed 2-way FSI model was applied for comparison of speed-line predictions for cold and hot analyses of the 1.41% cold-tip-clearance configuration as well as for identification of flow features associated with the NPSMF.

## A. SPEED-LINE PREDICTION

Prediction of a 90% speed-line was conducted using generated meshes for the gas-path and rotor geometries with mesh statistics documented in Table 5. Further mesh refinement for speed-line prediction was limited by computation resources and time available. A full list of applied settings for CFX-Pre was placed in Appendix H.

Table 5.    2-way FSI speed-line mesh statistics

|  | Gas Path (CFX) | Blade (ANSYS Mechanical) |
|---|---|---|
| Mesh Nodes | 1,173,670 | 304,667 |
| Mesh Elements | 3,595,317 | 197,683 |

### 1. Blade Deformation

Blade-deformation results for the 2-way FSI at the same near-peak efficiency conditions as used for the 1-way FSI solution are shown in Figure 13 and Figure 14 with tabulated results placed in Table 6 with the 1-way results for comparison. Deformation trends for the 2-way FSI largely matched those results seen for the 1-way FSI solution, but with an additional amount of deformation due to fluid forces. This additional deformation was 2 orders of magnitude lower than the deformation due to 1-way FSI alone.
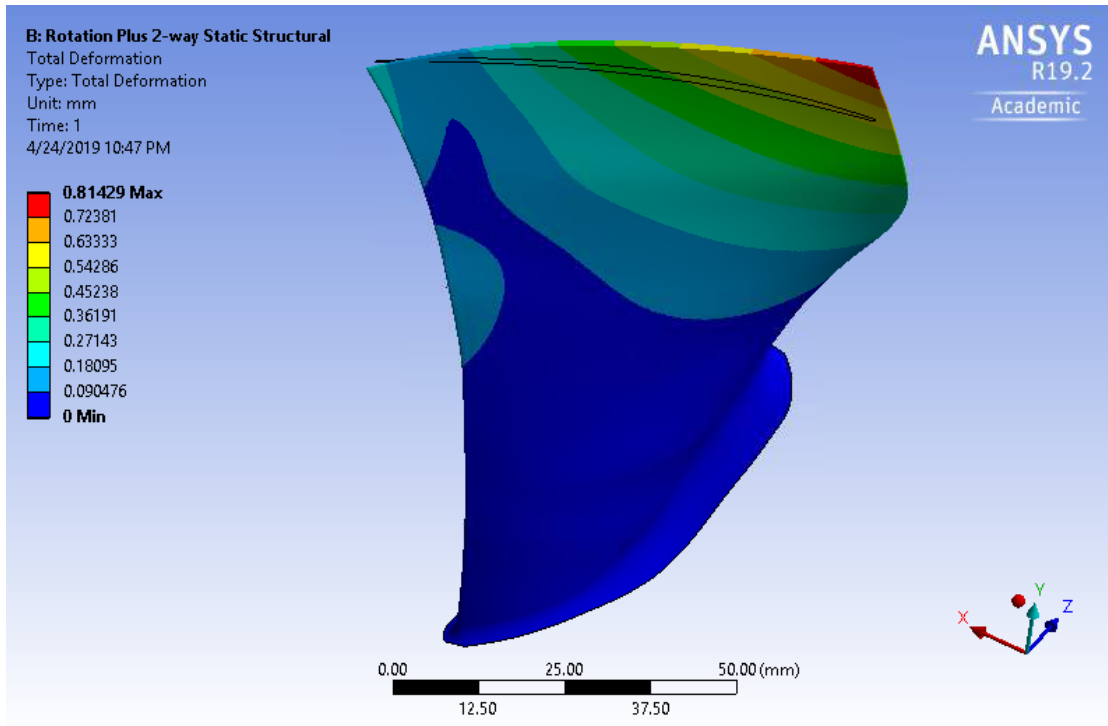
Figure 13.    Total deformation due to 2-way FSI
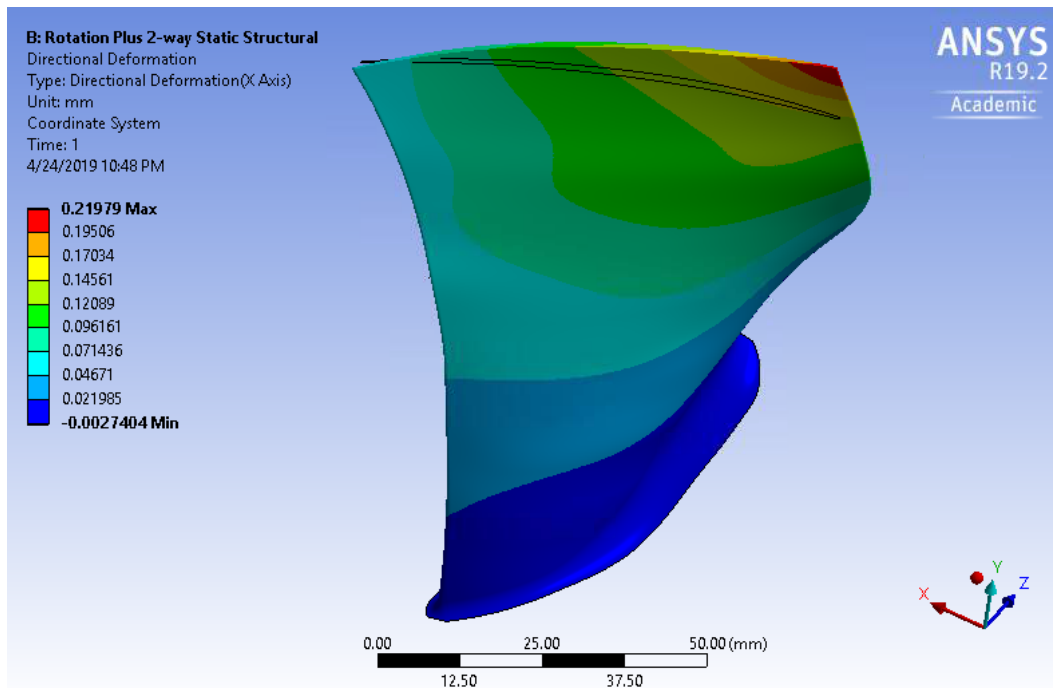


Figure 14.    Radial deformation due to 2-way FSI

Table 6.    Blade-deformation results for 2-way FSI

| Deformation | Rotation only | 1-Way FSI Only | Rotation + 1-Way FSI | 2- Way FSI |
|---|---|---|---|---|
| Max Total | 0.88304 mm (TE) (0.034765 in) | 0.18721 mm (LE) (0.0073706 in) | 0.81495 mm (TE) (0.032085 in) | 0.81429 mm (TE) (0.032059 in) |
| Max Radial | 0.23404 mm (TE) (0.0092141 in) | 0.0098912 mm (LE) (0.00038942 in) | 0.21986 mm (TE) (0.008656 in) | 0.21979 mm (TE) (0.0086531 in) |
| Total LE | 0.14775 mm (0.0058169 in) | 0.18721 mm (0.0073706 in) | 0.23563 mm (0.0092768 in) | 0.24730 mm (0.0097361 in) |
| Radial LE | 0.036406 mm (0.0014333 in) | 0.0098912 mm (0.00038942 in) | 0.045724 mm (0.0018002 in) | 0.045774 mm (0.0018021 in) |
| Total TE | 0.88304 mm (0.034765 in) | 0.073507 mm (0.0028940 in) | 0.81495 mm (0.032085 in) | 0.81429 mm (0.032059 in) |
| Radial TE | 0.23404 mm (0.0092141 in) | -0.014179 mm (-0.00055821 in) | 0.21986 mm (0.008656 in) | 0.21979 mm (0.0086531 in) |

## 2.    Total Pressure Ratio

Predicted pressure-ratio performance for cold and hot analyses were plotted alongside experimental data in Figure 15. Both hot and cold analyses demonstrated stall margins greater than those seen in experimental tests. This was attributed to over prediction of efficiencies as discussed in the next section as well as the use of a steady-state fluid analysis. Flow at near-stall conditions is largely unsteady and aperiodic; thus, an unsteady analysis of the entire rotor is required for appropriate modeling of rotor stall. Hot analyses consistently increased modeling fidelity as compared to cold analyses. Hot analyses directly matched experimental data in the near-stall region. In the near-peak efficiency region, hot analyses reduced the number of experimental error margins from approximately 4 to approximately 2.6 as compared to cold analyses. At choke, the hot analyses were within approximately 1.3 error margins. These shifts in predictions directly affirm the improvements anticipated through implementation of a 2-way FSI. Further improvements could be made through implementation of a full-blisk structural model as well as increased mesh refinement especially near flow features such as shocks and in the tip-gap region.
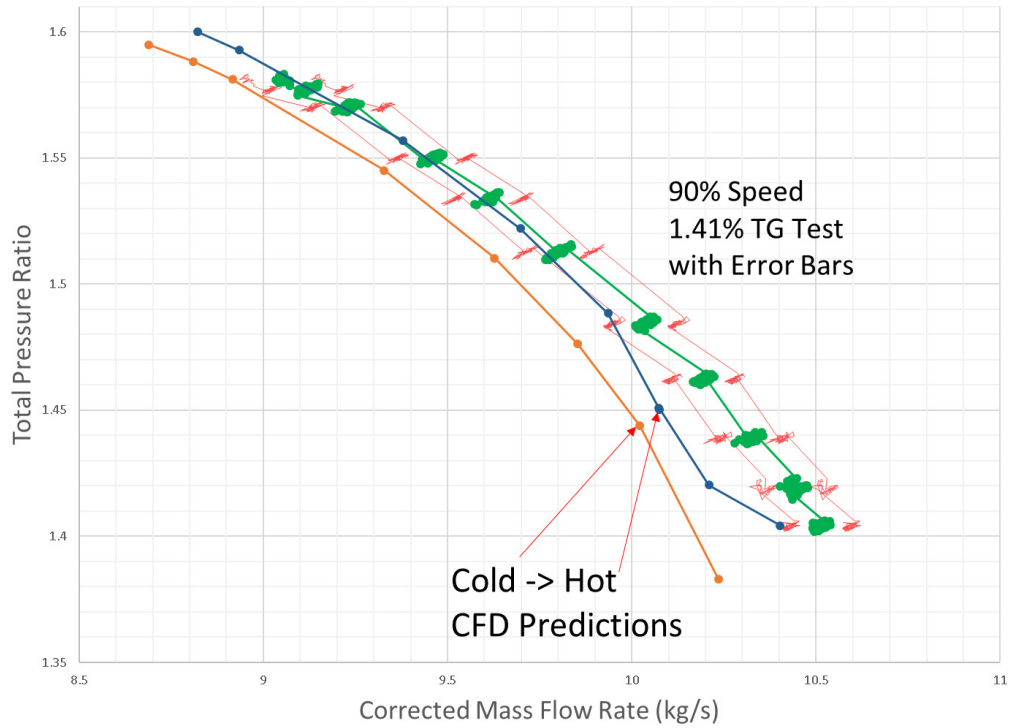
Figure 15.   Total pressure ratio for 2-way FSI

### 3.    Isentropic Efficiency

Predicted isentropic efficiencies for cold and hot analyses were plotted alongside experimental data in Figure 16. Cold and hot analyses both were seen to overpredict experimental efficiencies. This may be attributed to the adiabatic assumptions applied to the CFX analyses as well as other losses not captured by the current fluid solution. Hot analyses showed a shift towards experimental data as shown by the reduction in predicted peak efficiency from 86.4% to 85.2% as compared to the experimental peak of approximately 81%. Further research is required to define and apply modeling improvements such as appropriate boundary conditions and increased meshing to better characterize efficiency-based performance of a transonic rotor.
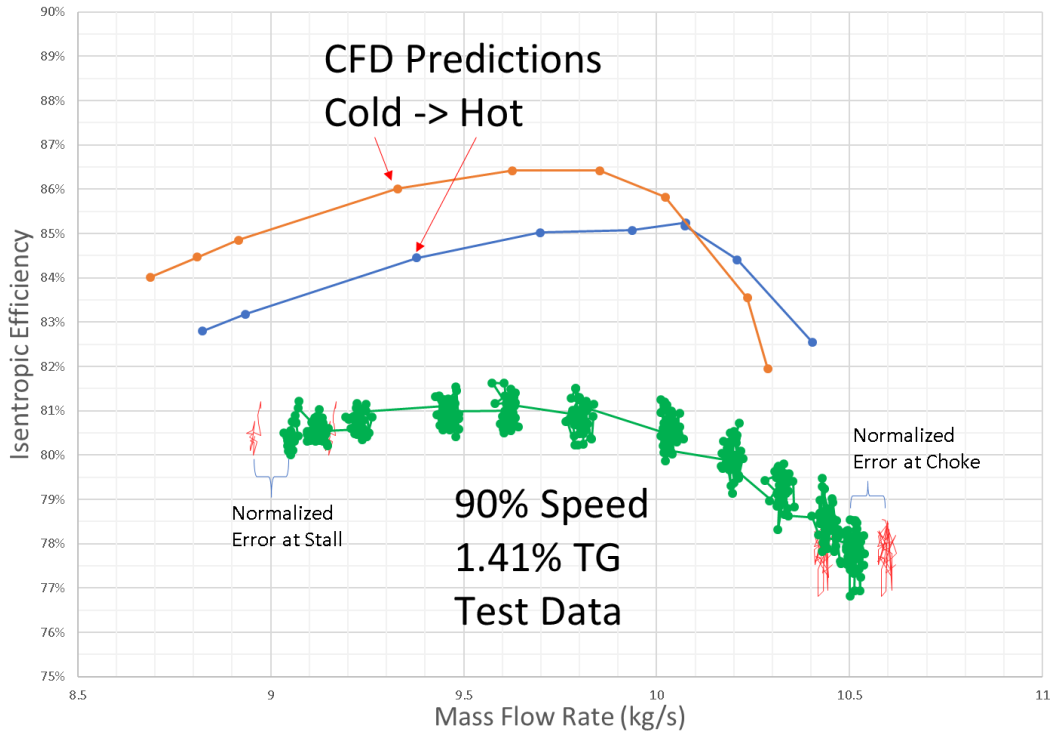
Figure 16.    Isentropic efficiency for 2-way FSI

## B.        FLOW-FEATURE IDENTIFICATION

An inherent advantage of the use of CFD for evaluation of fluid solutions is the ability to visualize and quantify flow phenomena not easily observable in experimental evaluation. To visualize flow features associated with the NPSMF and understand how rotor deflection effects performance predictions, a high-resolution mesh was developed and applied for the same near-peak efficiency boundary conditions used in discussion of 1-way and 2-way FSI rotor deflections. Flow features associated with the NPSMF and changes due to rotor deflection are discussed in this section.

### 1.        Meshing

Meshes of the gas-path and of the blade for flow-feature identification were constructed as shown by the gas-path mesh displayed in Figure 17 and mesh statistics in Table 7. The blade mesh was too refined for reasonable imaging and thus omitted from this report. The meshing approach for flow-feature identification involved mesh refinement of

27

the rotor-blade edges in the gas path and further refined edges for the mesh in ANSYS Mechanical. This approach ensured modeling fidelity of the curvature of the blade as the blade deforms. Thus, the developed mesh has a greatly increased ratio of nodes to elements as compared to the mesh in the cold-shape analysis.
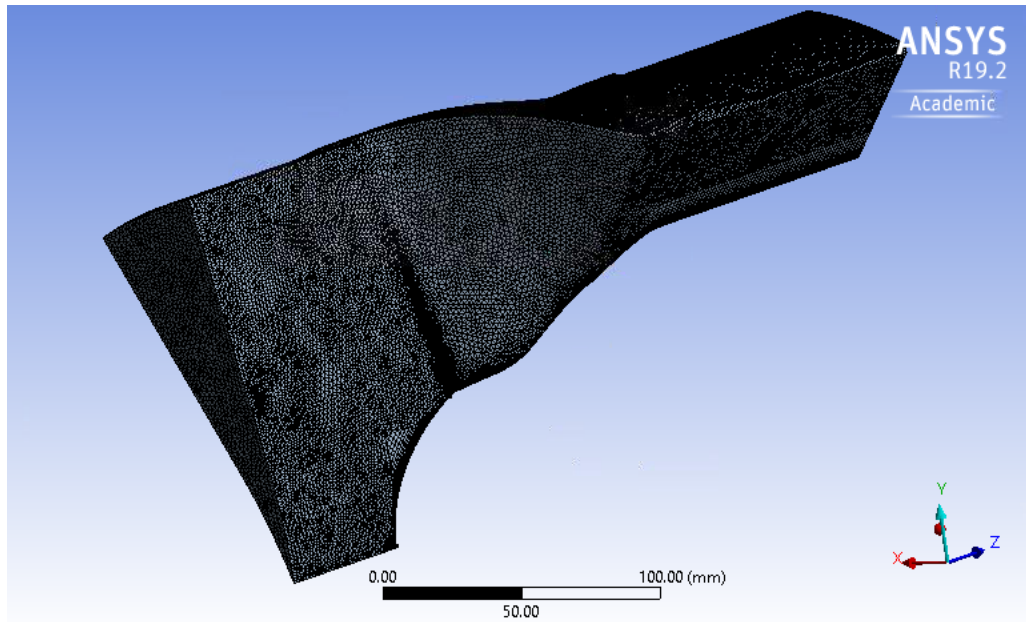


Figure 17.   Gas-path mesh for flow-feature identification, 1.41% tip-gap

Table 7.   Flow-feature-identification mesh statistics

|  | Gas Path (CFX) | Blade (ANSYS Mechanical) |
|---|---|---|
| Mesh Nodes | 16,218,793 | 3,787,639 |
| Mesh Elements | 7,149.793 | 2,485,926 |

Additional care was implemented to model the tip-gap region as shown by a cross-section of the mesh in Figure 18. Inflation layers were refined based upon preliminary solution y+ values, resulting in the y+ values documented in Table 8 for a near-peak efficiency data point. Further refinement was limited by computational resources and time available as well as inherited geometric features of the developed gas path.
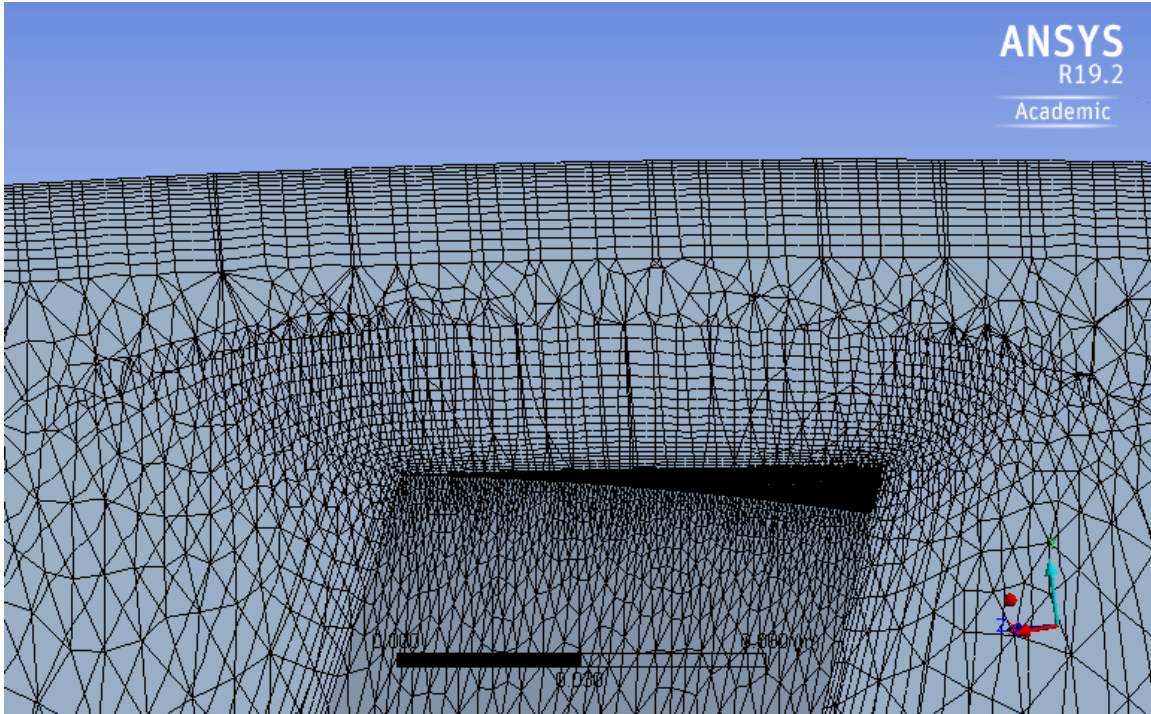
Figure 18.　Cross section of 1.41% tip-gap mesh for 2-way FSI

Table 8.　Selected y+ values for flow-feature-identification mesh

| Region | Rotor Blade | Casing | Outer Walls | Inner Wall | Blisk Nose |
|---|---|---|---|---|---|
| Area Average y+ | 7.39251 | 6.95461 | 8.11748 *average | 17.1581 | 6.76447 |
| Max y+ | 17.3904 | 10.2545 | 221.654 | 23.7843 | 115.102 |
| Min y+ | 0.565155 | 0.718817 | 0.225872 | 6.12437 | 0.225553 |

### 2.　Rotor-Blade Shock Systems

Pressure contours of the high- and low-pressure sides of a blade for the NPSMF were created and placed in Figure 19. These allowed for primary identification of flow features effecting the performance and deflection of blades for the NPSMF. Primary identification was aided through implementation of a Mach 1 isosurface with pressure contours as shown in Figure 20. Pressure spikes were anticipated to be associated with shocks occurring through the test section due to the transonic-flow regime. These two plots

allowed for preliminary identification of a bow/normal shock, a normal shock mid-way through the blade passage, and a normal shock at the outlet of the blade passage.
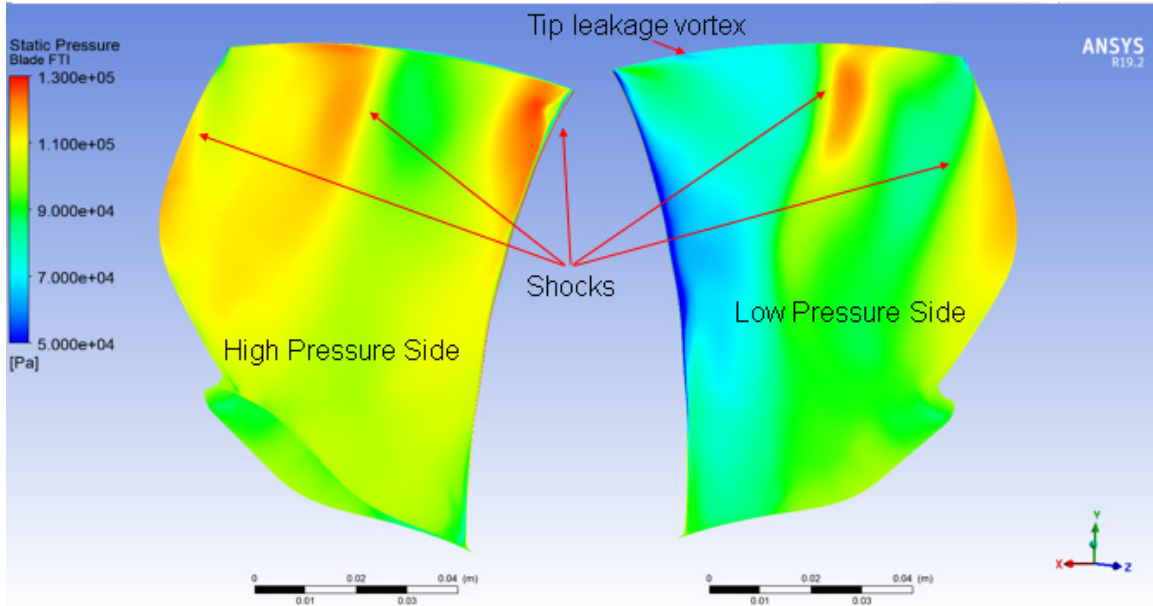


Figure 19.   Blade pressure contours for hot shape, 1.41% tip-gap
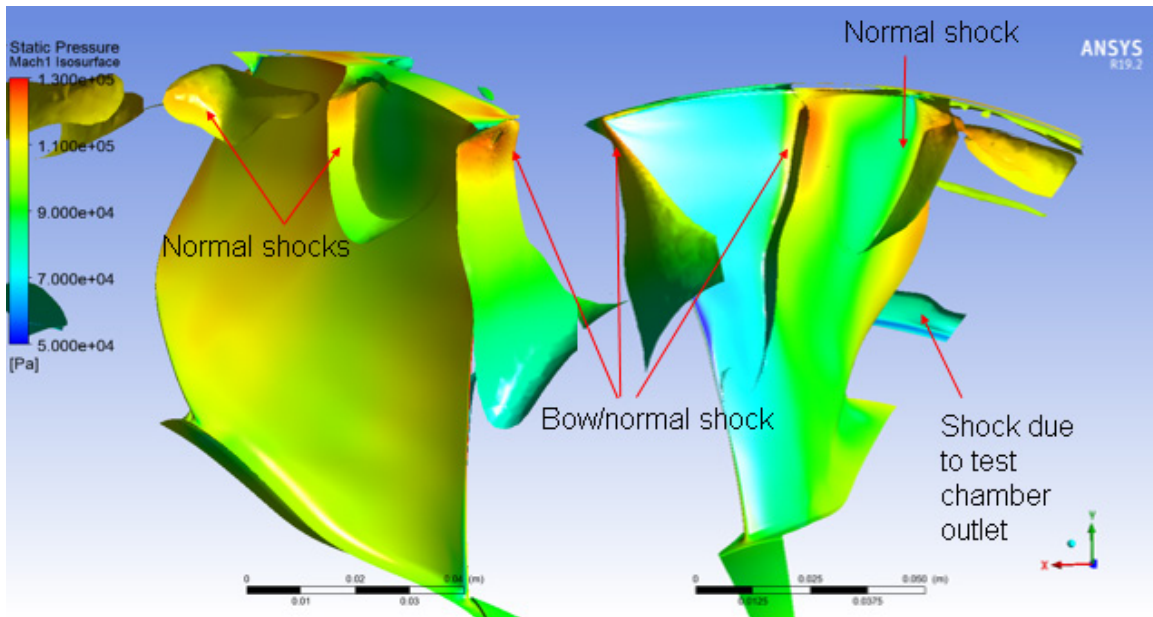


Figure 20.   Mach 1 isosurface, pressure contours for hot shape, 1.41% tip-gap

Further visualization of the shock systems associated with the NPSMF involved placing a pressure-contour surface at 91% of the blade span as shown in Figure 21.
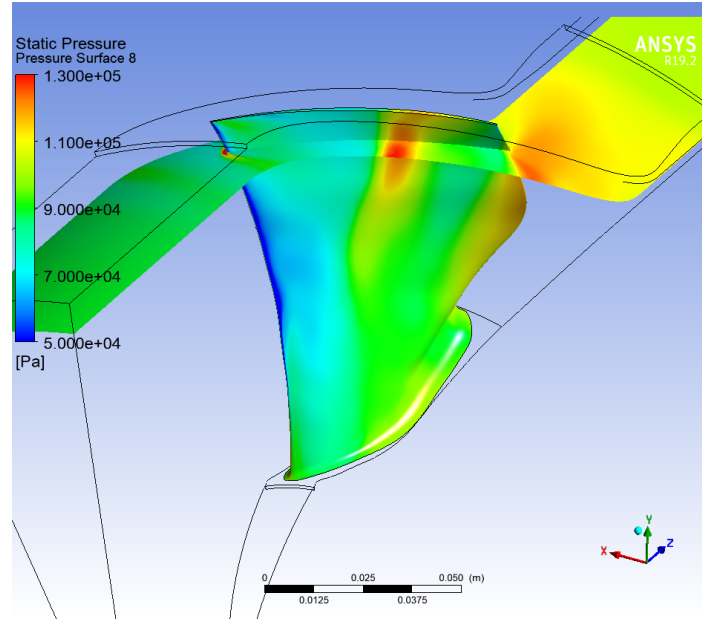


Figure 21.    Blade-passage pressure-contour location, hot shape, 1.41% tip-gap

The pressure-contour surface shown in Figure 21 was placed in Figure 22 with zoomed in contours of pressure and Mach number at the rotor-blade LE placed in Figure 23. These images demonstrate how a bow shock from each blade also functions as a normal shock mid-chord on the low-pressure side of each preceding blade. Also, a normal shock originating mid-chord along the high-pressure side of each blade also functions as a normal shock at the TE of the low-pressure side of each preceding blade. Finally, a normal shock occurs at the TE of the high-pressure side of each blade. Analysis of the rotor's LE shows expansion from stagnation to supersonic flow on both high- and low-pressure sides of the blade with a small shock occurring on the high-pressure side.
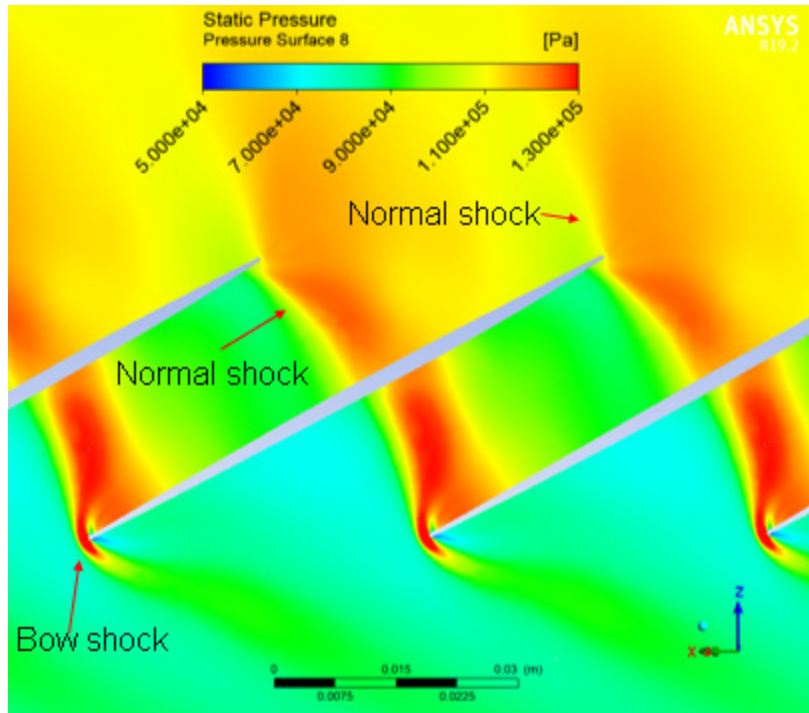
Figure 22.   Hot pressure contours with annotated shocks, 1.41% tip-gap
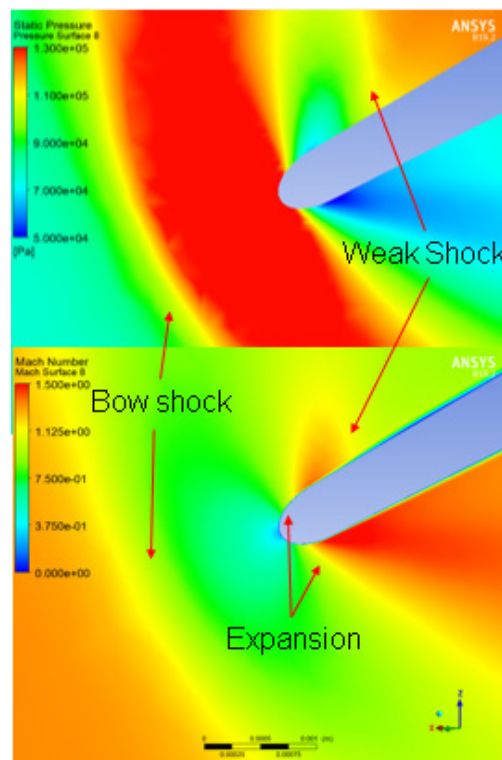


Figure 23.   Hot blade LE pressure and Mach number, 1.41% tip-gap

### 3. 2-Way FSI Effects

Pressure contours for hot- and cold- analyses of the NPSMF at the same location as Figure 22 were placed in Figure 24. Comparison of these pressure contours shows similar shock structures with increased pressure spikes and differing LE shocks for the hot analysis. As previously discussed with 2-way FSI deformation results, the fluid loads deflect the LE of the blade while rotational loads "untwist" the rotor blade. These deformations cause an increase in mass flow and changed angle of incidence for the rotor. Increased mass flow increases the relative Mach number, increasing the pressure spike associated with normal shocks. The changed angle of incidence was attributed as the main cause for differences in the secondary shock on the high-pressure side at the LE.
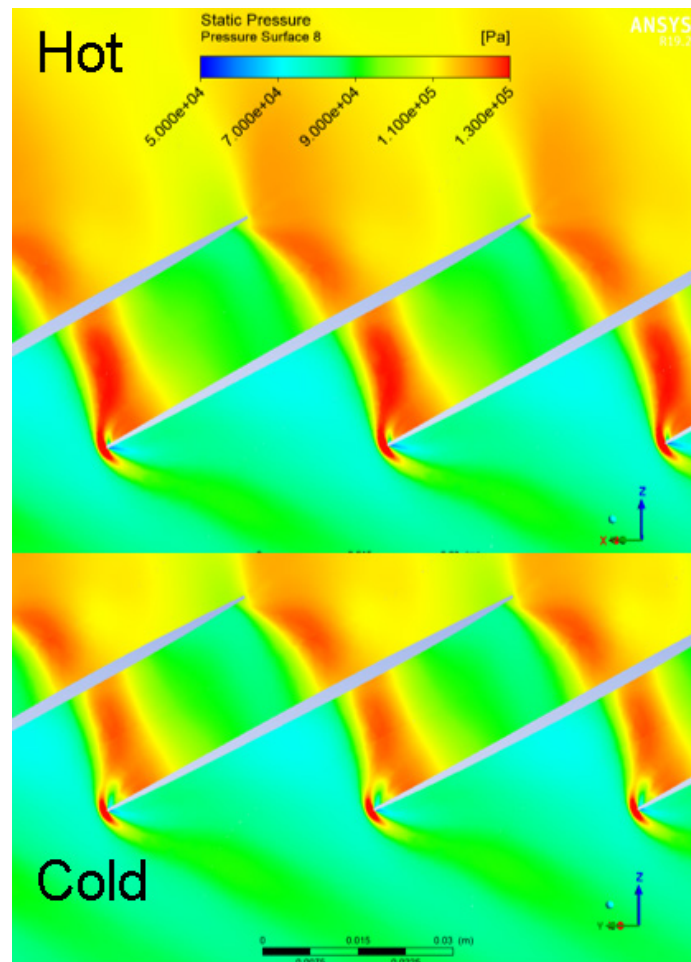


Figure 24.    Pressure contours for hot and cold analyses, 1.41% tip-gap

## 4. Test-Section Outlet Mach Bubble

A flow feature unique to the TCR test section was identified through application of pressure and Mach-number contours at the periodic boundary conditions as shown in Figure 25. This flow feature was identified to be a section of the flow where Mach number peaked at 1.244 due to convergence of the test section downstream of the rotor. This was identified as a Mach bubble where flow goes supersonic for a small region and subsequently shocks back to the subsonic flow regime. This has implications on recorded pressure-based performance of the NPSMF as experimental results may not be reflective of rotor-only performance if the rotor were to be implemented in a different test section. Evaluation of this flow phenomena and thus prediction of experimental results could be improved through better meshing in the outlet region especially at the point of test-section constriction.
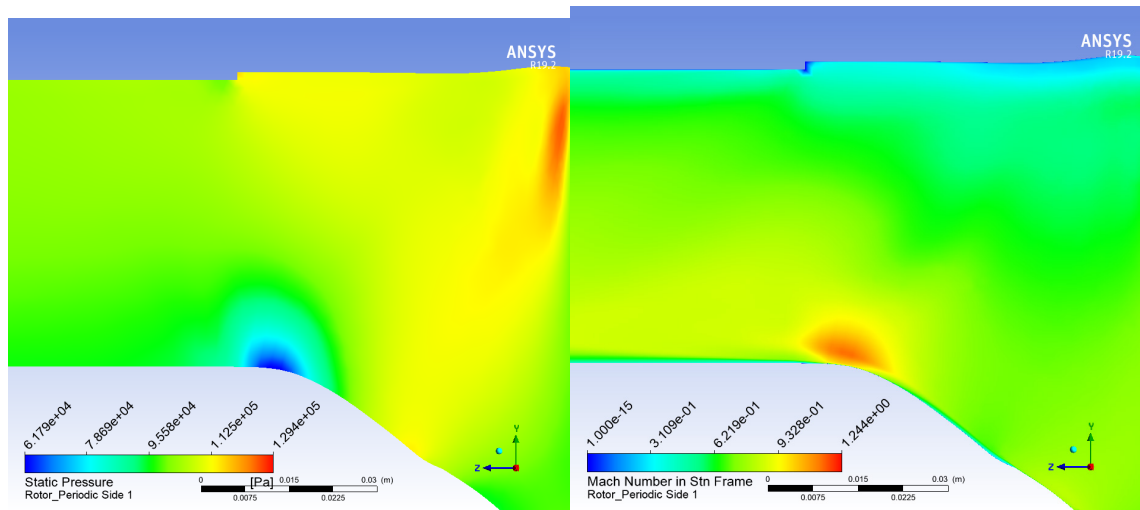


Figure 25.    Outlet Mach bubble pressure and Mach number, 1.41% tip-gap

## 5. Tip-Leakage Vortex

Tip-leakage vortices are caused by the pressure gradient at the tip of the rotor blade causing air to flow over the rotor tip and inducing rotation. These flow phenomena can induce adverse effects including stall initiation and degradation of efficiency for the rotor

[5]. The tip vortex for the NPSMF is visualized in Figure 26 and Figure 27 using streamlines and pressure contours at the rotor-blade tip.
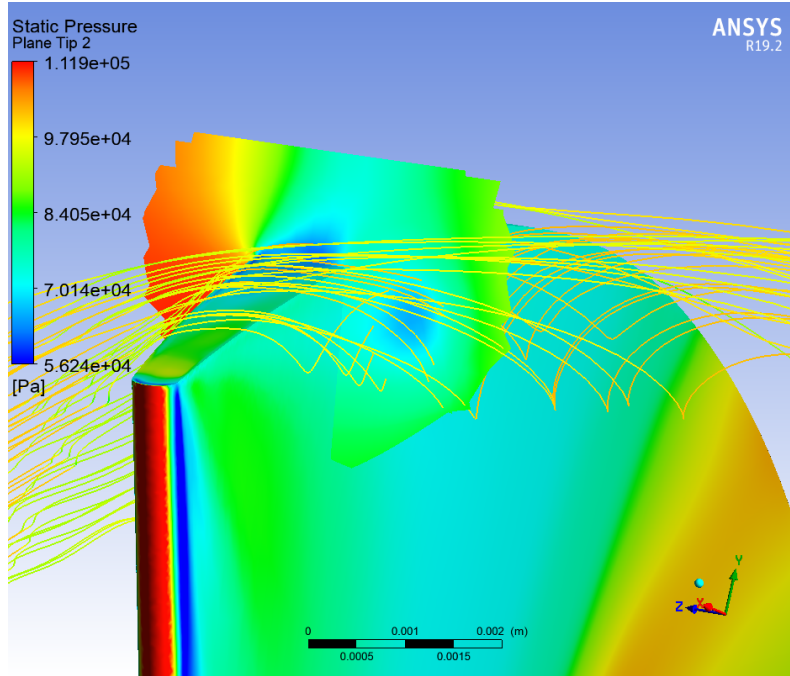


Figure 26.   Hot shape tip-leakage vortex pressure contour, 1.41% tip-gap
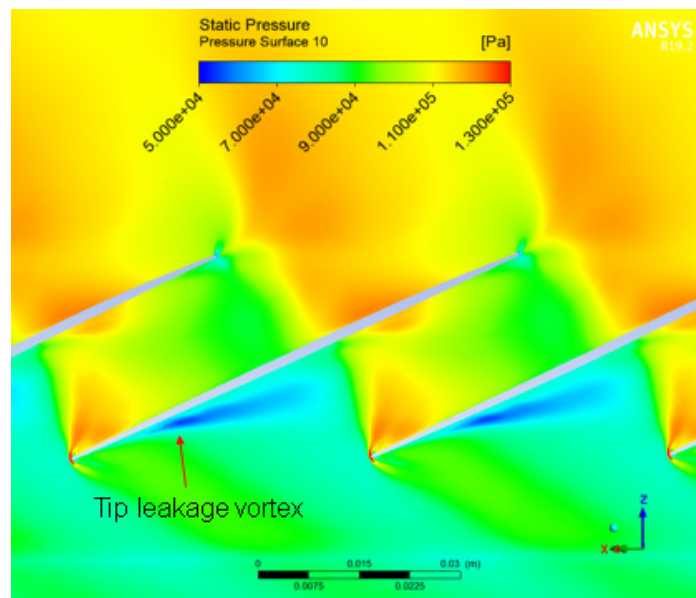


Figure 27.   Hot pressure contour at blade tip, 1.41% tip-gap

35

THIS PAGE INTENTIONALLY LEFT BLANK

# VII. CONCLUSIONS AND RECOMMENDATIONS

## A. CONCLUSIONS

This study sought to improve CFD modeling fidelity of the NPSMF through implementation of a 2-way FSI. Hot-shape fluid analyses showed matching of pressure-ratio experimental data in the near-stall region and improved CFD modeling fidelity elsewhere as compared to cold-shape analyses for the same mesh. CFD analyses also allowed for identification of flow features such as the rotor-blade shock systems, the tip-leakage vortex, and the test-section outlet Mach bubble.

The developed 2-Way FSI modeling approach may be further implemented as an effective supplement to experimental data for pressure-ratio performance prediction for alternative rotor configurations or alternative rotors. Further research is required for CFD to replace experimental values for the mass-flow range and isentropic efficiencies as the developed model over predicts peak-efficiency values by approximately 4%.

## B. RECOMMENDATIONS

Further research into implementation of a 2-way FSI may include implementation of adaptive meshing. This would allow for increased capability in capturing shock and wake effects without the burden of extreme refinement of the entire fluid domain, effectively increasing modeling fidelity at a much lower computational cost. However, CFX currently does not allow for implementation of adaptive meshing while mesh motion is enabled, while there is an external solver coupled to the solution, or while there is an interface enabled such as periodic conditions such as those used in this study. As such, if CFX adaptive meshing remains inhibited by these capabilities, a whole blisk cold-shape analysis would have to be used first with adaptive meshing, then the adapted mesh would somehow need to be used in the 2-way FSI coupling. Meshing may also be improved through application of additional metrics beyond y+ to measure mesh fidelity as y+ only evaluates a small portion of the domain.

The structural model for 2-way FSI could be greatly improved through expanding the structural analysis to that of the rotor blisk rather than just the rotor blade. This would

remove the faults associated with the fixed-root boundary conditions seen in this study, but would require research into implementation of hub growth and how an axisymmetric assumption may be applied for a structural model in ANSYS Mechanical. If the axisymmetric assumption cannot be applied, a whole blisk fluid model would have to be applied which would require significant computational resources to maintain CFD modeling fidelity.

Boundary conditions may be improved through implementation of a corrected mass-flow boundary condition. This may allow for increased fidelity in modeling of outlet pressure profiles as opposed to the current average pressure profile, which constrains the pressure profile based upon a blending factor.

# APPENDIX A. MASS-FLOW MEASUREMENT NOZZLE MODEL

Calculation of mass-flow rate for the TCR is done by measuring stagnation pressure and temperature of inlet air as well as static pressure at the flow rate nozzle. Based upon these three parameters, mass-flow rate can be calculated using compressible isentropic flow relations defined by an "X" or stagnation velocity approach.

$$X_1 = \sqrt{1 - \left(\frac{P_1}{P_{t1}}\right)^{\frac{(\gamma-1)}{\gamma}}}$$

$$\dot{m}_{ideal} = \left(1 - X_1^2\right)^{\frac{1}{(\gamma-1)}} X_1 A \frac{P_{t1}}{R} \sqrt{\frac{2C_p}{T_{t1}}}$$

This calculated theoretical mass-flow rate is then related to the experimental mass-flow rate by use of a discharge coefficient ($C_D$) which is the direct ratio of the two.

$$C_D = \frac{\dot{m}_{exp}}{\dot{m}_{ideal}}$$

Traditionally, testing of the TCR utilized a constant value for $C_D$ of 1.03. As test data repeatedly gave higher values for mass flow than those predicted by CFD analysis, this value was brought into question.

To investigate the $C_D$ value for the flow rate nozzle used by the TCR, a series of studies were conducted using CFX. The SST turbulence model with a gamma-theta transitional turbulence model was used over a series of design points that varied mass-flow rate at the outlet of the flow nozzle and inlet stagnation pressure. Inlet stagnation temperature was held to a constant 288.15 K. The resultant $C_D$ values were plotted against Reynolds number and Mach number based upon mass-flow nozzle port pressure measurements in Figure 28 and Figure 29. These plots showed limited dependency upon inlet stagnation conditions for the discharge coefficient until higher Mach numbers were reached.
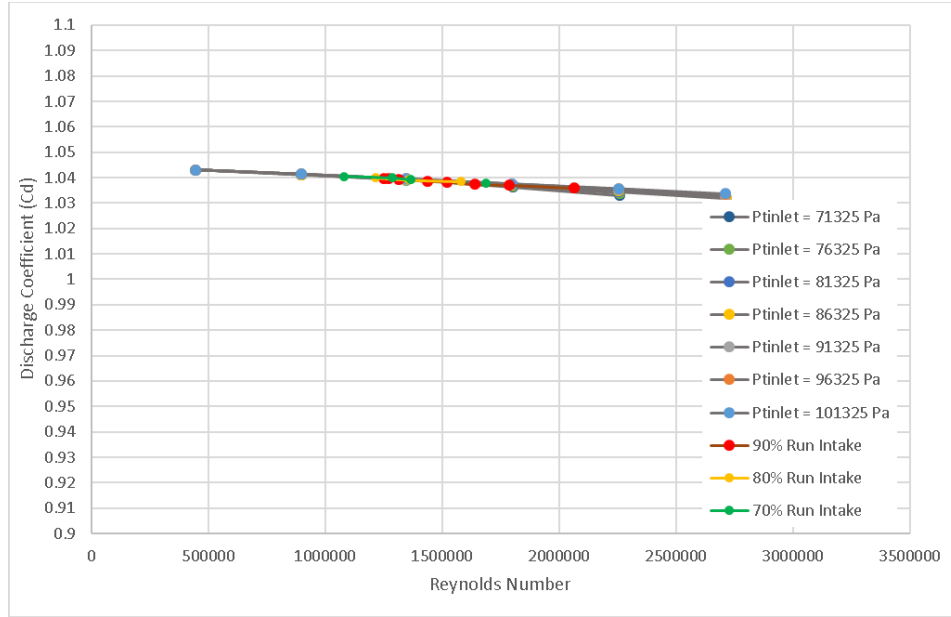
Figure 28.     Discharge coefficient versus Reynolds number
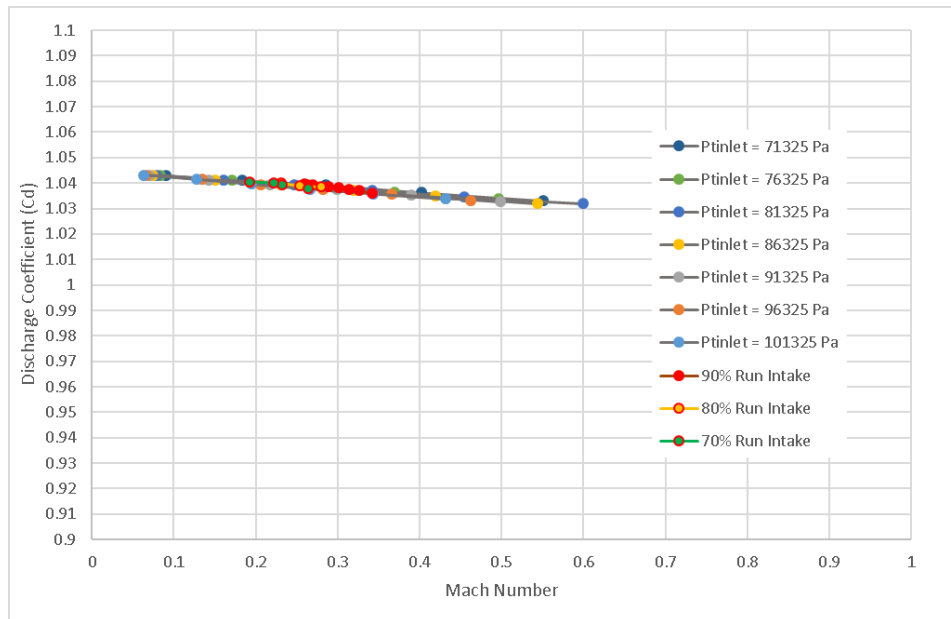


Figure 29.     Figure 1. Discharge coefficient versus Mach number

For a practical calibration equation, actual mass-flow rate was plotted against ideal mass-flow rate in Figure 30. This collapsed the data into a linear trend that was then quantified according to the linear regression line plotted with the data. The linear regression

line was set to have a zero intercept value to quantify a directly proportional relationship between the two mass-flow rates. The CFD results predict a standard $C_D$ value of 1.035793 according to the applied linear regression line through the origin. This verified the utilized discharge coefficient value of 1.03 for testing.
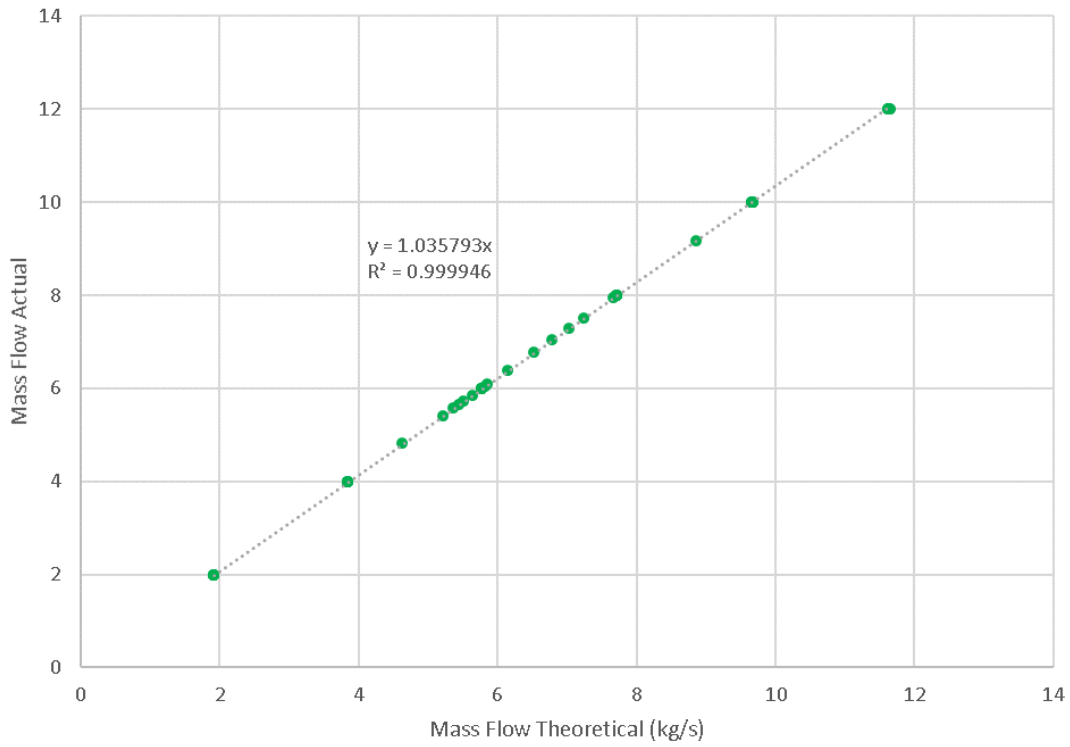


Figure 30.    Comparison of actual to ideal mass-flow rates

THIS PAGE INTENTIONALLY LEFT BLANK

# APPENDIX B. MASS-FLOW ERROR ANALYSIS

An error analysis of the mass-flow data-acquisition process was conducted to determine the normalized error at each data point. The normalized error is defined by relating each of the recorded parameters ($P_n$) in test to the scaled mass-flow rate ($\dot{m}_s$) where ($\Delta P_n$) is the tolerance for the nth measured parameter.

$$\frac{\Delta \dot{m}_s}{\dot{m}_s} = \frac{1}{\dot{m}_s}\left(\frac{\partial \dot{m}_s}{\partial P_1}\Delta P_1 + \frac{\partial \dot{m}_s}{\partial P_2}\Delta P_2 + \cdots + \frac{\partial \dot{m}_s}{\partial P_n}\Delta P_n\right)^{1/2}$$

The mass-flow data-acquisition process begins with recording total temperature ($T_{t1}$), total pressure ($P_{t1}$), and static pressure ($P_1$) port measurements at the mass-flow nozzle and using an "X" or stagnation velocity formulation to calculate the ideal mass-flow rate ($\dot{m}_{ideal}$).

$$X_1 = \sqrt{1 - \left(\frac{P_1}{P_{t1}}\right)^{\frac{(\gamma-1)}{\gamma}}}$$

$$\dot{m}_{ideal} = \left(1 - X_1^2\right)^{\frac{1}{(\gamma-1)}} X_1 A \frac{P_{t1}}{R}\sqrt{\frac{2C_p}{T_{t1}}}$$

This mass-flow rate is then corrected by the discharge coefficient ($C_D$) to obtain the actual experimental mass-flow rate ($\dot{m}_x$).

$$\dot{m}_x = C_D \dot{m}_{ideal}$$

This is then scaled to reference conditions using average measured inlet stagnation temperature ($T_{o1,avg}$) and inlet stagnation pressure ($P_{o1,avg}$) at the inlet for the tested rotor. This calculation results in a referred mass-flow rate ($\dot{m}_{ref}$).

$$\theta_{ref} = \frac{\gamma R T_{o1,avg}}{\gamma_{ref} R_{ref} T_{ref}}; T_{ref} = 288.15K$$

43

$$\delta_{ref} = \frac{P_{o1,avg}\gamma}{P_{ref}\gamma_{ref}}; P_{ref} = 1atm$$

$$\gamma_{ref} = 1.4; R_{ref} = 287\frac{J}{kg \cdot K}$$

$$\dot{m}_{ref} = \frac{\dot{m}_x\sqrt{\theta_{ref}}}{\delta_{ref}}$$

This mass-flow rate is then scaled based upon the actual RPM and intended RPM for the test in question to give $\dot{m}_s$.

$$\dot{m}_s = \frac{\dot{m}_{ref}RPM_{intend}}{RPM_{ref}}; RPM_{ref} = \frac{RPM_{test}}{\sqrt{\theta_{ref}}}$$

Excluding gas constants $\gamma$, $C_p$, and $R$, there are 6 parameters that effect the measurement of the scaled mass-flow rate: $P_1$, $P_{t1}$, $T_{t1}$, $P_{o1,avg}$, $T_{o1,avg}$, and $RPM_{test}$. The partial derivatives and assumed tolerances for each are given by the following relations.

$$\frac{\partial\dot{m}_s}{\partial P_1} = \dot{m}_s \cdot \frac{1}{\gamma P_{t1}}\left[\left(1-X_1^2\right)^{\frac{(\gamma-2)}{(\gamma-1)}} - \frac{(\gamma-1)}{2\left(1-X_1^2\right)^{\frac{1}{(\gamma-1)}}X_1^2}\right]; \Delta P_1 = 86.16Pa$$

$$\frac{\partial\dot{m}_s}{\partial P_{t1}} = \dot{m}_s \cdot \frac{(\gamma-1)}{\gamma P_{t1}}\left[1+\frac{1-X_1^2}{2X_1^2}\right]; \Delta P_{t1} = 86.16Pa$$

$$\frac{\partial\dot{m}_s}{\partial T_{t1}} = \frac{-\dot{m}_s}{2T_{t1}}; \Delta T_{t1} = 1K$$

$$\frac{\partial\dot{m}_s}{\partial P_{o1,avg}} = \frac{-\dot{m}_s}{P_{o1,avg}}; \Delta P_{o1,avg} = 86.16Pa$$

$$\frac{\partial\dot{m}_s}{\partial T_{o1,avg}} = \frac{\dot{m}_s}{T_{o1,avg}}; \Delta T_{o1,avg} = 1K$$

$$\frac{\partial\dot{m}_s}{\partial RPM_{test}} = \frac{-\dot{m}_s}{RPM_{test}}; \Delta RPM_{test} = 10RPM$$

The results of this analysis were applied to test data for the 70, 80, and 90% speed-lines to obtain error bars such as those shown in Figure 3. The overall range of test data gave a 0.8% normalized error at the highest speeds and 2.1% at the lowest speeds.

THIS PAGE INTENTIONALLY LEFT BLANK

# APPENDIX C. ANSYS WORKBENCH PARAMETERIZATION

Previous numerical evaluation of a speed-line at the TPL involved developing a workbench model that was compatible with a series of MATLAB and python codes that were used to automate the process of changing boundary conditions for a single workbench file. This process utilized the parameterization tool inherent to Workbench. The approach utilized in this research skipped the MATLAB and python codes and directly utilized the Workbench design point tools. These tools create and manipulate many individual Workbench projects through the manipulation of user-defined inputs, and populate a spreadsheet of user-defined outputs. The procedure for and some notes on lessoned learned from this process are shown here.

## A.     INPUT PARAMETER INITIALIZATION

In order for the parameters cellblock to appear in Workbench, a parameter must be initialized within a cellblock in a given Workbench structure. To do this in the Setup block of a CFX fluid solver structure, first open the Setup block. Then add an expression with a defined value and appropriate units. Finally, right click that expression and select "Use as Workbench input parameter." This will lock the expression from further manipulation within CFX-pre and add a Parameters cellblock in Workbench. The parameter's value now may only be manipulated by opening the Parameter Set tab in Workbench by opening the Parameters cellblock. An example of this process is shown in Figure 31 and Figure 32.
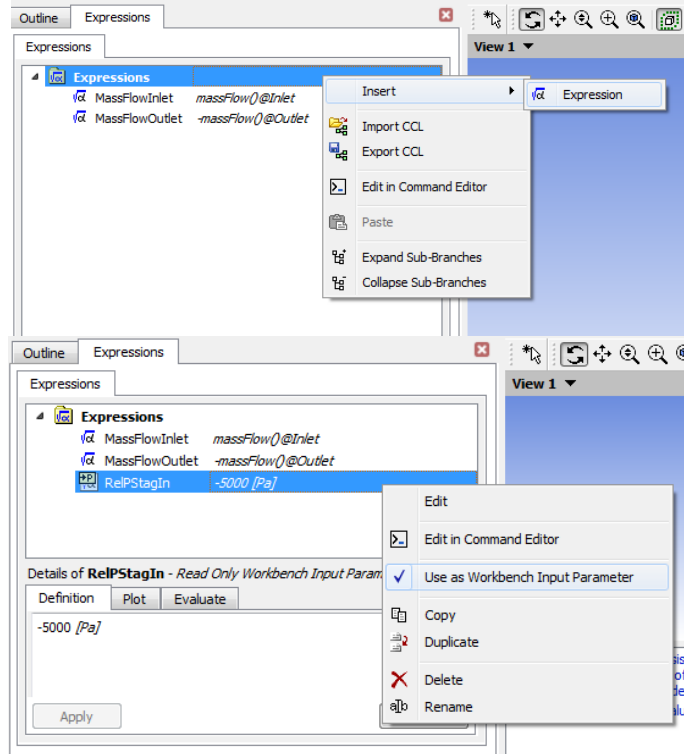
Figure 31.    Creating a Workbench input parameter in CFX-Pre
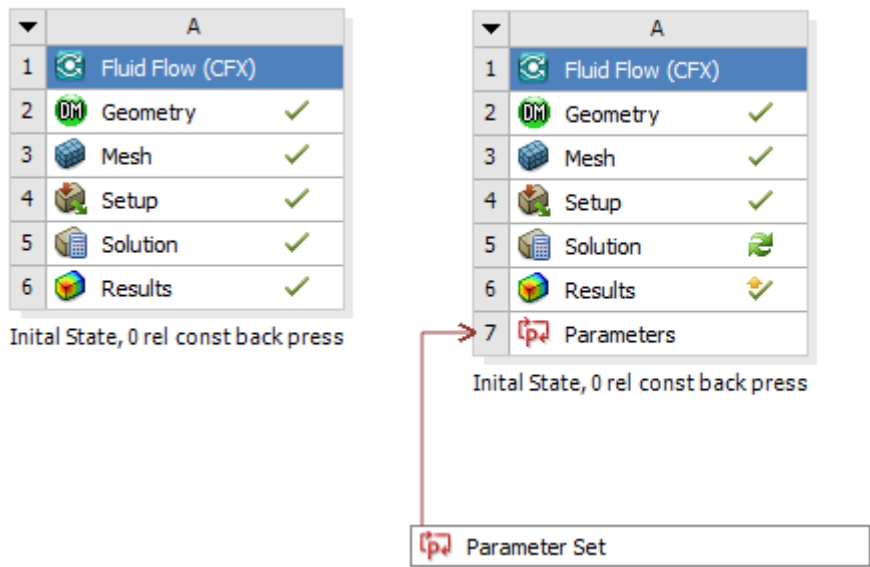


Figure 32.    Workbench before and after input parameter initialization

Each design point that is created will update its respective Workbench project with the respective input parameters that are defined. Thus, it pays off to parameterize as much as possible to enable full manipulation of the solution for each design point. Parameterization is not limited to CFX-pre. For example, it is also possible to parameterize various items in Meshing through clicking the checkboxes next to parameter inputs, or do much of the same in ANSYS Mechanical. This enables rapid manipulation of the whole Workbench project without having to wait for initialization of each program prior to parameter modification.

## B.    OUTPUT PARAMETER INITIALIZATION

Output parameterization is conducted much the same as input parameters, but is generally only practical in the results component of a given solution. First, create an expression that is desired to be observed as an output. Then denote that expression as an output parameter for Workbench. In the CFX-Post, this is done by right-clicking the expression and selecting the option "Use as Workbench output parameter." This will lock the expression and add its value to the Design Point spreadsheet in the Parameter Set tab of Workbench.
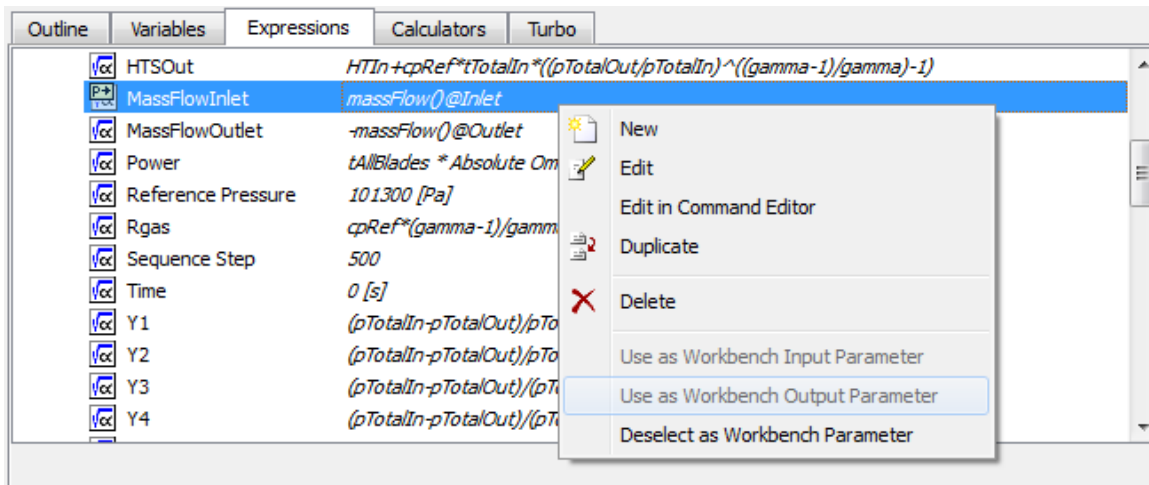


Figure 33.    Set Workbench output parameter in CFX-Post

Of note, input parameters may be specified in CFX-Post; these may be necessary if one of the input parameters for CFX-Pre does not transfer directly to solution data and is necessary for calculations. Examples of expressions or values to utilize for output parameters are: state values (Ex. Mass-flow averaged inlet/outlet stagnation pressure), calculated values (Ex. Efficiencies, pressure ratio, corrected mass flow), and values that quantify fidelity or convergence of the solution (Ex. Area averaged Y+ for each domain, inlet versus outlet mass flow). It is advantageous to parameterize as much of the output as possible, especially if it is decided not to retain solution data for every design point.

## C. PARAMETER SET TAB

Once one or more parameters are initialized, the Parameters cellblock will appear in the workbench structure. The Parameter Set tab for either the entire Workbench project or the individual solver block can be accessed by selecting the respective Parameters cellblock. The Parameters Set tab provides a description with units of each defined parameter, a Design Point Table, and the ability to chart selected parameters.
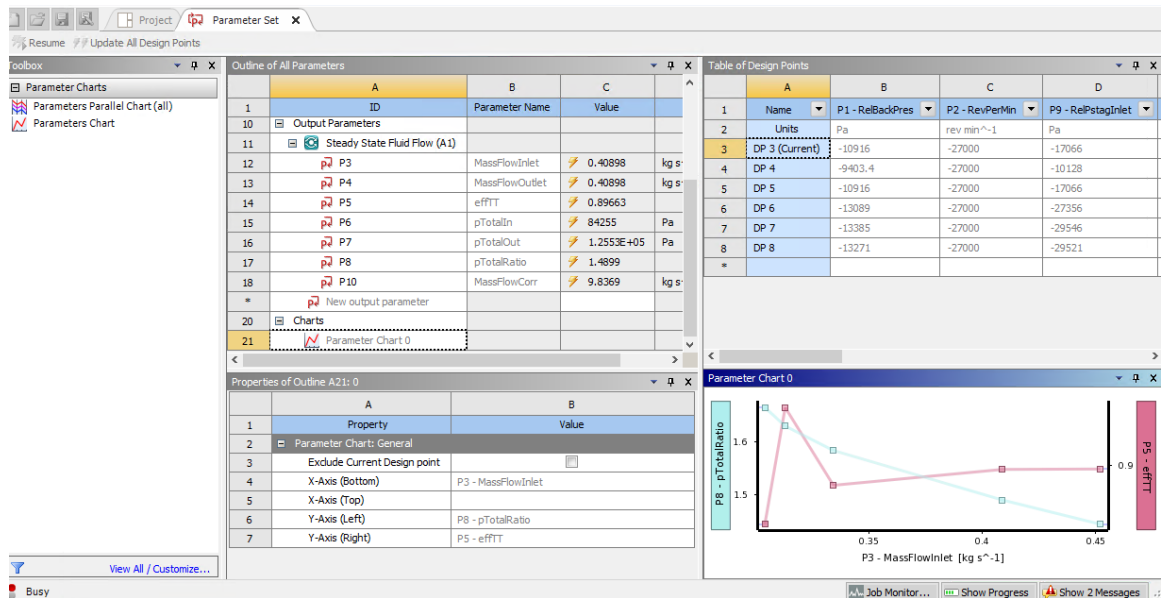


Figure 34.   Parameters set tab

The Design Point Table allows for modification of input parameters for a given design point and reading of output parameters as design points are updated. Each design point functions as its own workbench project that is the result of updating based upon the "Current" design point or based upon the "Previous Updated" design point. The update order may be seen, modified, or "optimized" based upon Workbench's preferences by right-clicking the design point number. This will add an update order column to the design point table. Effective manipulation of the update order may be necessary for quality results pending the variations in input parameters.

Results from the parameters may be plotted versus design point number or versus other parameters. This allows for intermediate viewing of the output parameter trends on at least two different axes (Ex. Plotting both pressure ratio and efficiency versus corrected mass-flow rate for iterative enhancement of mesh resolution). To observe results from a specific retained design point, simply right-click the design point and make it the current design point. Then return to the project schematic to open the respective design point's results. Note: if anything is modified in the results component of the project, all other design points will require an update. For non-retained design points, this could remove all output data. Thus, be sure to save the project before observing results in CFX-Post.

To export a specific design point as an individual workbench project, right click the design point and click export selected design points. This can be a useful tool for sharing results without having to send the entire collection of design points, which can be a rather large collection of data. It can be useful to export particular design points of interest throughout the project design process to avoid overwriting results and retain the ability to easily view those results in CFX-Post.

## D.    ADDITIONAL NOTES

As each design point is essentially an entirely new Workbench project, the disc space cost of an expansive design point spreadsheet can be quite costly and be prone to errors after modifications, for example, of CFX-Post. Thus, it is recommended to only use a small number of design points (Ex. < 5 or just 1 if possible) until the project structure is finalized and particular output parameters defined before running an expansive set of

simulations. After that point, exporting specific design points will greatly reduce load times for opening and analyzing results that are non-numerical (Ex. Chart plots of outlet stagnation pressure distribution versus radius) and will reduce the likelihood of cellblocks not being marked as updated.

Update order can be a valuable tool or cause failure in some simulations. Consistently be aware of which option (Update from "Current" or "Previous Updated") is being used and how this can be used to the advantage of domain initialization (I.E. apply gradually increases/decreases in rotation speed rather than large jumps at near-choke or near-stall conditions). One possible use of the update order would be to first run simulations for near-peak efficiency or mid-speed-line at each speed, and then rearrange update order so those are the initial conditions for calculation of their respective simulations.

# APPENDIX D. USING ANSYS SYSTEM COUPLING FOR FSI

Previous FSI studies at the TPL utilized ANSYS Multifield to couple the fluid and structural solvers. As of ANSYS Workbench 19, Multifield has been removed from the CFX solver, and the System Coupling block must be used. This appendix discusses the application of System Coupling as used in this study.

## A. SETUP STEPS

Basic setup for System Coupling involves creating individual data sources and solvers and linking them to the System Coupling block in Workbench. In the case where solvers are both co-solving a solution as in this study, the setup blocks for each solver are connected to the setup of the System Coupling block. For a 1-way data transfer such as a 1-way FSI, the solution block of the individual component is linked to the setup of System Coupling.

Within the individual solvers for FSI, the fluid interaction surface must be identified. In the case of CFX, mesh deformation must be enabled and the FSI surface must have the deformation source defined as "System Coupling." For ANSYS Mechanical, a fluid-interaction must be defined. Then, two data transfers must be created in the System Coupling block: force from the CFX surface to the Mechanical surface, and mesh deformation from the Mechanical surface to the CFX surface. Each of these data transfers may then have convergence criteria, under-relaxation factors, and ramping settings defined as desired.

Only steady coupled analyses were conducted in this study. Setup of solver steps and staggering here thus only apply to steady analyses. The method for solver staggering involved defining number of stagger iterations and stagger order in System Coupling. The number of individual solver iterations per stagger iteration was defined in the solver settings in CFX-pre. Each stagger iteration would run CFX to convergence or to the defined number of iterations in CFX-pre. Solver partitioning was defined in the individual solvers.

During a run, a select range of convergence monitors is available within the System Coupling tab of Workbench. These are limited to data transfer convergence, data transfer

values, CFX residuals, and any pre-defined monitors in ANSYS Mechanical. To monitor values defined in CFX-Pre, a CFX solver window must be opened to monitor the run in progress.

## B.     ADDITIONAL NOTES

In regards to mesh deformation, it was found that simply enabling mesh deformation in the CFX at the transonic regime for this rotor gave divergence or false convergence of mass flows. If this is encountered, it is recommended to set the "meshdisp diffusion scheme" expert parameter to 4. This applies a blended scheme for the interior of the mesh and a central scheme for the boundaries of the mesh. The default is a setting of 2 which applies positive definite coefficients for the interior when solving mesh displacement equations. For more information, see "Mesh Displacement Diffusion Scheme" (Sec. 5.1.5) in the *CFX Reference Guide* [6] and "Discretization Parameters" (Sec. 17.3.1) in the *CFX-Solver Modeling Guide* [7].

Many measures are available to limit the likelihood of mesh folding or negative volume elements. It is recommended to linearly ramp the mesh deformation data transfer over a series of coupling steps to distribute the deformation due to rotation. Under relaxation factors may also be applied to the data transfer, but were not for this study. Boundary conditions in CFX may also be modified to allow for structured mesh deformation for stationary boundaries such as the rotor casing. In this study, the mesh for the rotor casing was allowed to deform as a surface of revolution to limit mesh shearing in the tip-gap region. Periodic boundary conditions may be allowed to have a conservative interface flux of mesh deformation, but this setting was not enabled for this study.

The approach for defining iteration numbers and convergence criteria for this study involved first doing a 1-way FSI to approximate the iterations to convergence (Ex. 300). This number was then truncated to less than a third of that value (Ex. 80) which was defined as the number of CFX iterations per step. Convergence criteria were modified to include a conservation criterion of 0.001 as residuals tended to converge much faster than mass flows. System coupling iterations were then defined to allow for linear ramping through approximately 10 coupling iterations with at least 4 follow-on coupling iterations to allow

for convergence of all components in the 2-way FSI. Convergence criteria for the data transfers may also need to be lowered depending on the simulation.

THIS PAGE INTENTIONALLY LEFT BLANK

# APPENDIX E. COLD-SHAPE CFX SETUP REPORT

1. Mesh Report

**Table 1.** Mesh Information for Fluid

| Domain | Nodes | Elements |
|---|---|---|
| Default Domain | 3,605,192 | 9,404,749 |

2. Physics Report

**Table 2.** Domain Physics for Fluid

| Domain - Default Domain | |
|---|---|
| Type | Fluid |
| Location | B127 |
| *Materials* | |
| Air Ideal Gas | |
| Fluid Definition | Material Library |
| Morphology | Continuous Fluid |
| *Settings* | |
| Buoyancy Model | Non Buoyant |
| Domain Motion | Rotating |
| Alternate Rotation Model | Off |
| Angular Velocity | RevPerMin |
| Axis Definition | Coordinate Axis |
| Rotation Axis | Coord 0.3 |
| Reference Pressure | 1.0000e+00 [atm] |
| Heat Transfer Model | Total Energy |
| Include Viscous Work Term | On |
| Turbulence Model | SST |
| Transitional Turbulence | Gamma Theta Model |
| Transition Onset Correlation | Langtry Menter |
| Turbulent Wall Functions | Automatic |
| High Speed Model | Off |
| **Domain Interface - Rotor_Periodic** | |
| Boundary List1 | Rotor_Periodic Side 1 |
| Boundary List2 | Rotor_Periodic Side 2 |
| Interface Type | Fluid Fluid |
| *Settings* | |
| Interface Models | Rotational Periodicity |
| Axis Definition | Coordinate Axis |
| Rotation Axis | Coord 0.3 |
| Mesh Connection | Automatic |

Expert Parameters:
Memory Control:
      Topology Estimate factor set to 1.15
High Speed Models:
      Max Continuity loops set to 3

**Table 3.** Boundary Physics for Fluid

| Domain | Boundaries | |
|---|---|---|
| Default Domain | **Boundary - Inlet** | |
| | Type | INLET |
| | Location | Inlet |
| | *Settings* | |
| | Flow Direction | Normal to Boundary Condition |
| | Flow Regime | Subsonic |
| | Heat Transfer | Stationary Frame Total Temperature |
| | Stationary Frame Total Temperature | 2.8815e+02 [K] |
| | Mass And Momentum | Stationary Frame Total Pressure |
| | Relative Pressure | RelPstagInlet |
| | Turbulence | Medium Intensity and Eddy Viscosity Ratio |
| | **Boundary - Rotor_Periodic Side 1** | |
| | Type | INTERFACE |
| | Location | Rotor_Periodic_1 |
| | *Settings* | |
| | Heat Transfer | Conservative Interface Flux |
| | Mass And Momentum | Conservative Interface Flux |
| | Turbulence | Conservative Interface Flux |
| | **Boundary - Rotor_Periodic Side 2** | |
| | Type | INTERFACE |
| | Location | Rotor_Periodic_2 |
| | *Settings* | |
| | Heat Transfer | Conservative Interface Flux |
| | Mass And Momentum | Conservative Interface Flux |
| | Turbulence | Conservative Interface Flux |
| | **Boundary - Outlet** | |
| | Type | OUTLET |
| | Location | Outlet |
| | *Settings* | |
| | Flow Regime | Subsonic |

| | | |
|---|---|---|
| Mass And Momentum | Average Static Pressure | |
| Pressure Profile Blend | 1.0000e-02 | |
| Relative Pressure | RelBackPres | |
| Pressure Averaging | Average Over Whole Outlet | |
| **Boundary - Blisk_Nose** | | |
| Type | WALL | |
| Location | F834.127, F1019.127, F1020.127, F1021.127, F1022.127, F112.127, F113.127, F114.127, F115.127, F116.127, F117.127, F118.127, F119.127, F120.127, F121.127, F122.127, F124.127, F125.127, F126.127, F276.127, F277.127, F824.127, F828.127, F832.127 | |
| *Settings* | | |
| Heat Transfer | Adiabatic | |
| Mass And Momentum | No Slip Wall | |
| Wall Roughness | Smooth Wall | |
| **Boundary - Wall** | | |
| Type | WALL | |
| Location | Wall, Casing | |
| *Settings* | | |
| Heat Transfer | Adiabatic | |
| Mass And Momentum | No Slip Wall | |
| Wall Velocity | Counter Rotating Wall | |
| Wall Roughness | Smooth Wall | |

THIS PAGE INTENTIONALLY LEFT BLANK

# APPENDIX F. NOTES FOR HIGH-SPEED CFX INITIALIZATION

During initial coarse CFX runs of the transonic rotor at 90% speed operation, the solver obtained a quasi-steady state solution that did not match experimental data. This solution was attained rapidly with a coarse mesh and could possibly give small enough residuals to exit the solver. Coarse-mesh solution data gave significantly lower mass flows, total pressure ratios, and efficiencies for the transonic rotor as compared to experimental data. With a medium mesh, the solver initially approached the coarse-mesh-solution, then the residuals and mass flows spiked before continuing convergence to an equilibrium solution that followed experimental values and trends.

Figure 35 and Figure 36 display the overlay of multiple mesh solutions with experimental data for the 90% speed-line and efficiency data. The quasi-steady state solution was found to drastically decrease mass-flow rate and total pressure ratios for the system as compared to the secondary solution and experimental data.
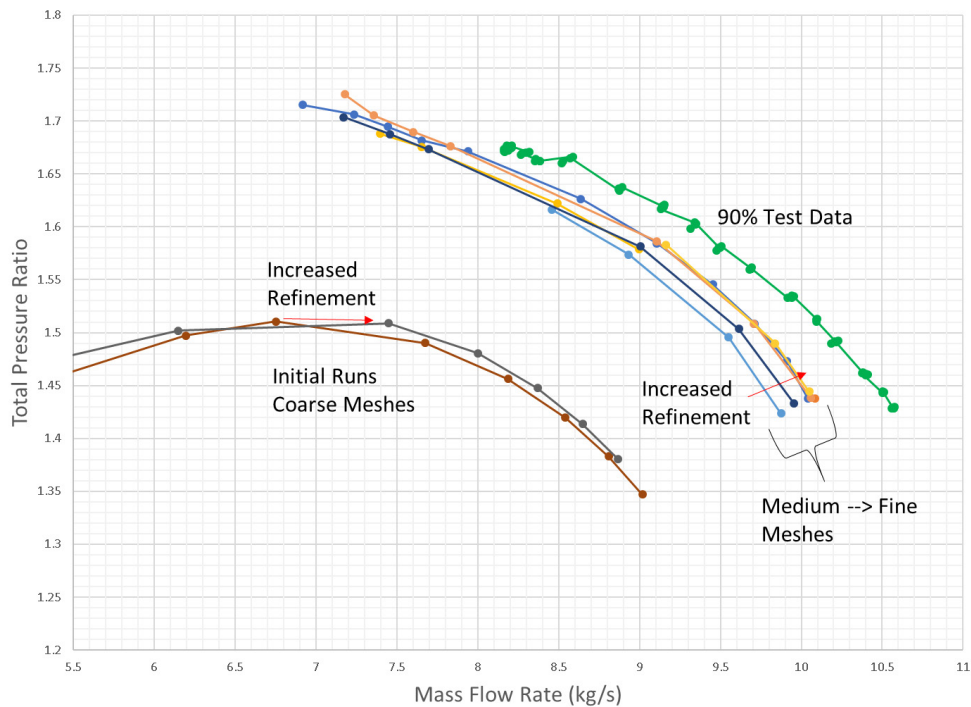


Figure 35.   90% speed operation pressure ratios

The primary attributed cause of this phenomenon was improper initialization of the domain. During experimentation, the rotor gradually increased speed up to the 90% speed condition, thus allowing shocks to develop with mass flow already established. By jumping straight to a 90% speed condition in CFX with only pressure-based initial conditions, the solver reached an intermediate, choked/stalled state with decreased mass flow and decreased efficiency. With increased iteration and a more fine mesh, the solver converged to a secondary steady-state solution that more closely matched experimental values and trends.
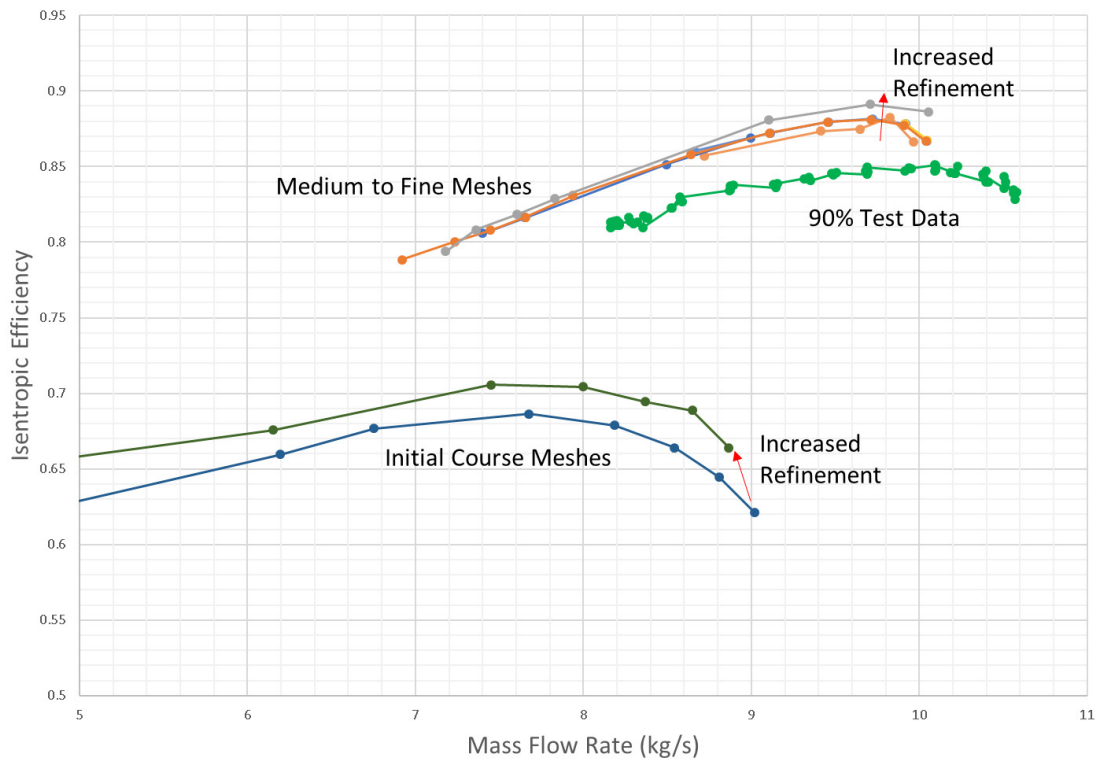


Figure 36.   90% speed operation efficiencies for experimental and CFX data

To prevent this issue for other transonic rotor simulations, it is recommended that adequate initialization of the domain occur. A good first step would be setting initial mass flow to that obtained in experiment. Another would be obtaining a low-speed solution, then iteratively increasing rotor speed and using the low-speed solution for the initial values of

the domain. If a high-speed solution is the only desired data point, run an medium mesh with a constant static-pressure outlet till the "spike" to the secondary solution is maintained, and then use that intermediate solution to define initial values for the fine mesh run with an average static-pressure outlet. Additionally, it is recommended that near-choke data points are initialized from near-stall data points to allow for development of transonic flow features. The bottom line is to think of how the experimental solution is obtained in practice and to correctly match that when setting up the CFX solver domain.

THIS PAGE INTENTIONALLY LEFT BLANK

# APPENDIX G. FLUID TURBULENCE MODEL SELECTION

Prior to conducting a 2-way FSI analysis at a full-scale mesh, a preliminary analysis was conducted to verify the use of the chosen turbulence model, SST with gamma-theta transitional model, over a more robust model such as k-epsilon. Mesh statistics are documented in Table 9.

Table 9.    Mesh statistics

|  | Gas Path (CFX) | Blade (ANSYS Mechanical) |
| --- | --- | --- |
| Mesh Nodes | 1,173,670 | 304,667 |
| Mesh Elements | 3,595,317 | 197,683 |

Preliminary data points were taken in the near-choke to peak efficiency regions of the 90% speed-line. Pressure ratio versus mass-flow rate is shown in Figure 37 for both cold and hot analyses at the coarse mesh for the k-epsilon and the SST with gamma-theta models. This plot demonstrates how the SST with gamma-theta transition model shifts the predicted performance towards experimental data, more than halving the steps of normalized error to the experimental data. Thus, the SST with gamma-theta transition was affirmed as having increased fidelity in modeling the given transonic rotor geometry and was chosen for use in the full-scale 2-way FSI discussed in this report. Additionally, the shift from cold to hot shape of the rotor blade predicts an increased mass-flow rate and higher pressure ratios, further shifting performance predictions towards experimental data and increasing fidelity. This provided preliminary affirmation of the positive impact a FSI has on the full-scale model predictions.
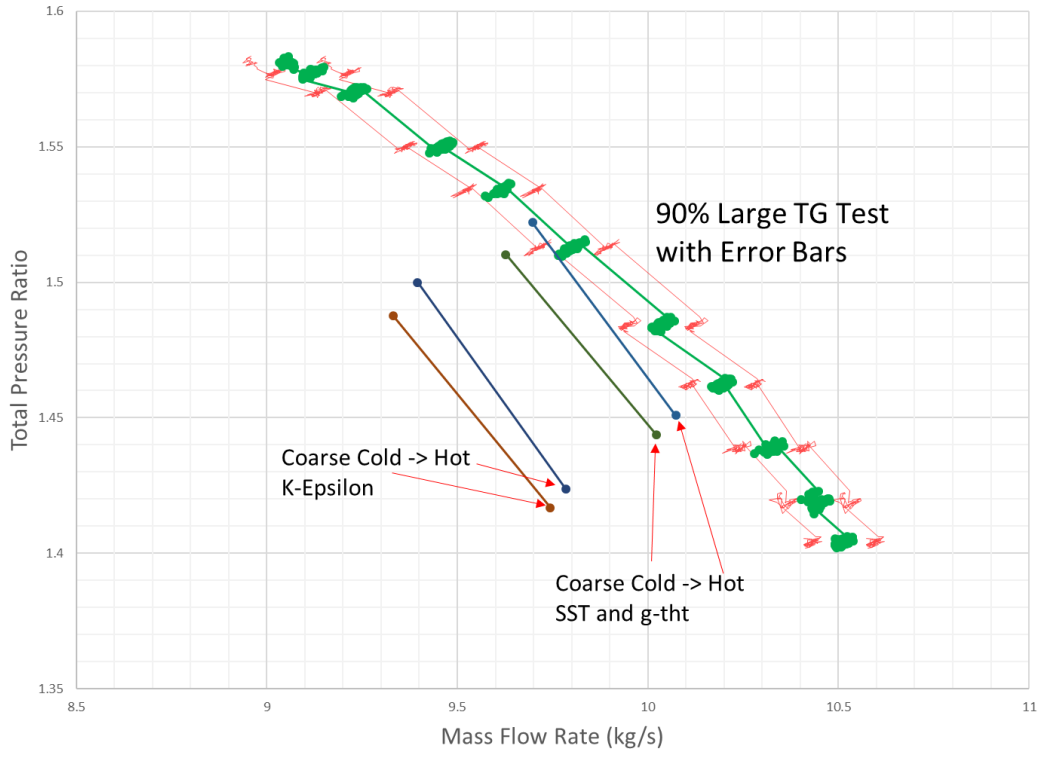
Figure 37.    Model comparison at coarse mesh

# APPENDIX H. 2-WAY FSI CFX SETUP REPORT

## 1. Mesh Report
**Table 1.** Mesh Information for Fluid

| Domain | Nodes | Elements |
|---|---|---|
| Default Domain | 16,218,793 | 7,149,793 |

*Mesh for flow feature identification

## 2. Physics Report
**Table 2.** Domain Physics for Fluid

| Domain - Default Domain | |
|---|---|
| Type | Fluid |
| Location | B127 |
| *Materials* | |
| Air Ideal Gas | |
| Fluid Definition | Material Library |
| Morphology | Continuous Fluid |
| *Settings* | |
| Buoyancy Model | Non Buoyant |
| Domain Motion | Rotating |
| Angular Velocity | RevPerMin |
| Axis Definition | Coordinate Axis |
| Rotation Axis | Coord 0.3 |
| Mesh Deformation | Regions of Motion Specified |
| Displacement Relative To | Previous Mesh |
| Mesh Motion Model | Displacement Diffusion |
| Mesh Stiffness | Blended Distance and Small Volumes |
| Reference Pressure | 1.0000e+00 [atm] |
| Heat Transfer Model | Total Energy |
| Include Viscous Work Term | On |
| Turbulence Model | SST |
| Transitional Turbulence | Gamma Theta Model |
| Transition Onset Correlation | Langtry Menter |
| Turbulent Wall Functions | Automatic |
| High Speed Model | Off |
| **Domain Interface - Rotor_Periodic** | |
| Boundary List1 | Rotor_Periodic Side 1 |
| Boundary List2 | Rotor_Periodic Side 2 |
| Interface Type | Fluid |
| *Settings* | |
| Interface Models | Rotational Periodicity |

| Axis Definition | Coordinate Axis |
|---|---|
| Rotation Axis | Coord 0.3 |
| Mesh Connection | Automatic |

Expert Parameters:
meshdisp diffusion scheme = 4

**Table 3.** Boundary Physics for Fluid

| Domain | Boundaries | |
|---|---|---|
| Default Domain | **Boundary - Inlet** | |
| | Type | INLET |
| | Location | Inlet |
| | *Settings* | |
| | Flow Direction | Normal to Boundary Condition |
| | Flow Regime | Subsonic |
| | Heat Transfer | Stationary Frame Total Temperature |
| | Stationary Frame Total Temperature | 2.8815e+02 [K] |
| | Mass And Momentum | Stationary Frame Total Pressure |
| | Relative Pressure | RelPStagIn |
| | Mesh Motion | Stationary |
| | Turbulence | Medium Intensity and Eddy Viscosity Ratio |
| | **Boundary - Rotor_Periodic Side 1** | |
| | Type | INTERFACE |
| | Location | Rotor_Periodic_1 |
| | *Settings* | |
| | Heat Transfer | Conservative Interface Flux |
| | Mass And Momentum | Conservative Interface Flux |
| | Mesh Motion | Stationary |
| | Turbulence | Conservative Interface Flux |
| | **Boundary - Rotor_Periodic Side 2** | |
| | Type | INTERFACE |
| | Location | Rotor_Periodic_2 |
| | *Settings* | |
| | Heat Transfer | Conservative Interface Flux |
| | Mass And Momentum | Conservative Interface Flux |
| | Mesh Motion | Stationary |
| | Turbulence | Conservative Interface Flux |
| | **Boundary - Outlet** | |
| | Type | OUTLET |
| | Location | Outlet |
| | *Settings* | |
| | Flow Regime | Subsonic |

| | |
|---|---|
| Mass And Momentum | Average Static Pressure |
| Pressure Profile Blend | 5.0000e-02 |
| Relative Pressure | RelBackPres |
| Mesh Motion | Stationary |
| Pressure Averaging | Average Over Whole Outlet |
| **Boundary - Blade FTI** | |
| Type | WALL |
| Location | Blade |
| *Settings* | |
| Heat Transfer | Adiabatic |
| Mass And Momentum | No Slip Wall |
| Wall Velocity Relative To | Mesh Motion |
| Mesh Motion | System Coupling |
| Wall Roughness | Smooth Wall |
| **Boundary - Blisk_Nose** | |
| Type | WALL |
| Location | Blisk minus Blade |
| *Settings* | |
| Heat Transfer | Adiabatic |
| Mass And Momentum | No Slip Wall |
| Wall Velocity Relative To | Mesh Motion |
| Mesh Motion | Stationary |
| Wall Roughness | Smooth Wall |
| **Boundary - Casing** | |
| Type | WALL |
| Location | F141.127 |
| *Settings* | |
| Heat Transfer | Adiabatic |
| Mass And Momentum | No Slip Wall |
| Wall Velocity Relative To | Boundary Frame |
| Wall Velocity | Counter Rotating Wall |
| Mesh Motion | Surface of Revolution |
| Axis Definition | Coordinate Axis |
| Rotation Axis | Coord 0.3 |
| Wall Roughness | Smooth Wall |
| **Boundary - Default Domain Default** | |
| Type | WALL |
| Location | F130.127, F134.127 |
| *Settings* | |
| Heat Transfer | Adiabatic |
| Mass And Momentum | No Slip Wall |
| Wall Velocity Relative To | Mesh Motion |

| | | |
|---|---|---|
| | Wall Velocity | Counter Rotating Wall |
| | Mesh Motion | Stationary |
| | Wall Roughness | Smooth Wall |
| | **Boundary - Inner Wall** | |
| | Type | WALL |
| | Location | Inner Wall |
| | *Settings* | |
| | Heat Transfer | Adiabatic |
| | Mass And Momentum | No Slip Wall |
| | Wall Velocity Relative To | Mesh Motion |
| | Wall Velocity | Counter Rotating Wall |
| | Mesh Motion | Stationary |
| | Wall Roughness | Smooth Wall |
| | **Boundary - Outer Wall** | |
| | Type | WALL |
| | Location | Outer Walls Minus Casing |
| | *Settings* | |
| | Heat Transfer | Adiabatic |
| | Mass And Momentum | No Slip Wall |
| | Wall Velocity Relative To | Mesh Motion |
| | Wall Velocity | Counter Rotating Wall |
| | Mesh Motion | Stationary |
| | Wall Roughness | Smooth Wall |

# LIST OF REFERENCES

[1]     E. V. DeSousa, "Development of advanced casing treatments for transonic compressors," M.S. thesis, MAE Department, Naval Postgraduate School, Monterey, CA, USA, 2018.

[2]     D. J. McNab, "Experimental testing and CFD modeling of an advanced transonic compressor for military applications," M.S. thesis, MAE Department, Naval Postgraduate School, Monterey, CA, USA, 2012

[3]     A. D. Terrell, "Transonic axial splittered rotor tandem stage," M.S. thesis, MAE Department, Naval Postgraduate School, Monterey, CA, USA, 2016.

[4]     G. L. Descovich, "Experimental and computational investigation of steam-induced stall in a transonic compressor rotor for a military fan," M.S. thesis, MAE Department, Naval Postgraduate School, Monterey, CA, USA, 2011.

[5]     C. Hah, D.C. Rabe, and A.R. Wadia, "Role of tip-leakage vortices and passage shock in stall inception in a swept transonic compressor rotor," *ASME Turbo Expo 2004: Power for Land, Sea, and Air,* American Society of Mechanical Engineers, 2004, pp. 545–555.

[6]     *ANSYS CFX Reference Guide Release 18.2*, ANSYS Inc., Canonsburg, PA, USA, 2018, Sec. 5.1.5. [Online]. Available: https://www.sharcnet.ca/Software/Ansys/18.2.2/en-us/help/cfx_ref/cfx_ref.html

[7]     *ANSYS CFX-Solver Modeling Guide Release 18.2*, ANSYS Inc., Canonsburg, PA, USA, 2018, Sec. 17.3.1. [Online]. Available: https://www.sharcnet.ca/Software/Ansys/18.2.2/en-us/help/cfx_mod/cfx_mod.html

THIS PAGE INTENTIONALLY LEFT BLANK

# INITIAL DISTRIBUTION LIST

1.      Defense Technical Information Center
        Ft. Belvoir, Virginia

2.      Dudley Knox Library
        Naval Postgraduate School
        Monterey, California